SLAC-J-ICFA-23
Fall 2001
SLAC-R-654

HOME PAGE

http://www.slac.stanford.edu/pubs/icfa/

ICFA INSTRUMENTATION BULLETIN*

The publication of the ICFA Instrumentation Bulletin is an activity of the Panel on Future Innovation and Development of ICFA (International Committee for Future Accelerators).

Volume 23

• Fall 2001 Issue

* Supported by the Department of Energy, contract DE-AC03-76SF00515.

ICFA INSTRUMENTATION BULLETIN

The publication of the ICFA Instrumentation Bulletin is an activity of the Panel on Future Innovation and Development of ICFA (International Committee for Future Accelerators). The Bulletin reports on research and progress in the field of instrumentation with emphasis on application in the field of high-energy physics. It encourages issues of generic instrumentation.

Publisher : Stanford Linear Accelerator Center
SLAC Publications Department
Stanford, CA 94309, U.S.A.

Editor : J. Va'vra

Web Technical Adviser : J. Schwiening

The views expressed in this Bulletin do not necessarily represent those of the ICFA Panel or the editor. In all cases, the authors are responsible for their manuscripts. The printed version is mailed out in limited numbers to institutions on the SLAC Instrumentation mailing list. Issues of the ICFA Instrumentation Bulletin are accessible electronically on our Web site:

http://www.slac.stanford.edu/pubs/icfa/

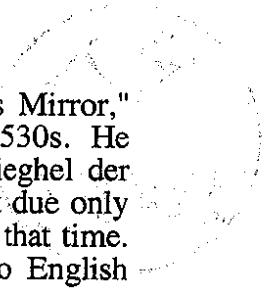

Cover: The illustration depicts L. J. Waghenaer's marine atlas, "The Mariner's Mirror," published in 1588. Lucas Janszoon Waghenaer was born in Holland in the 1530s. He became a famous ship pilot in his time. In 1584, he published the atlas ("Spieghel der Zeevaerdt") which was greatly valued among mariners for centuries. This was not due only to the map content, but also to the detailed knowledge of navigation techniques of that time. The atlas, as it appears on our page, is the same one used for the Dutch to English translation.

Conference List

- The third Beaune Conference on "New Developments in Photodetection," June 17-21, 2002. Web site: http://beaune.in2p3.fr.

- The fourth RICH Workshop on "RICH Detectors," Pylos, Greece, June 5-10, 2002.* Web site: http://www.nestor.org.gr/rich2002.

* Dedicated to the Memory of Tom Ypsilantis.

Table of Contents

A Large-Area Timing RPC

A. Blanco,[1,2] R. Ferreira-Marques,[1,3] Ch. Finck,[4] P. Fonte,[1,5,*]
A. Gobbi,[4] A. Policarpo,[1,3] M. Rozas.[2]

1. LIP, Coimbra, Portugal
2. GENP, Dept. Fisica de Particulas, Univ. de Santiago de Compostela, Spain
3. Departamento de Física da Universidade de Coimbra, Portugal
4. GSI, Darmstadt, Germany
5. ISEC, Coimbra, Portugal

Abstract

A large-area Resistive Plate Chamber (RPC) with a total active surface of 160×10 cm^2 was built and tested. The surface was segmented into two 5-cm wide strips readout on both ends with customized, very high speed, front-end electronics.

A timing resolution σ = 50-75 ps, with an efficiency for Minimum Ionizing Particles (MIPs) larger than 95%, was attained over the whole active area, in addition to the position resolution along the strips of 1.2 cm. Despite the large active area per electronic channel, the observed timing resolution is remarkably close to the one previously obtained (σ = 50 ps) with much smaller chambers of about 10 cm^2 area.

These results open the perspective of extending the application of timing RPCs to large-area arrays exposed to moderate particle multiplicities, where the low cost, good time resolution, insensitivity to the magnetic field, and compact mechanics may be attractive when compared with the standard scintillator-based Time-of-Flight (TOF) technology.

1 Introduction

The development of timing Resistive Plate Chambers (RPCs) [1] opened a possibility to build large-granularity high-resolution TOF systems with considerable cost reduction per channel when compared to standard scintillator-based technology.

Previous research has shown a timing resolution of better than 50 ps σ at 99% efficiency in single, four-gap chambers [2], and an average timing resolution of 88 ps σ with an average efficiency of 97% in a 32 channel system [3]. It has also been shown that each amplifying gap of 0.3 mm thickness has a detection efficiency of close to 75% and that the avalanche develops under the influence of a strong space charge effect [4]. A Monte Carlo model of the avalanche development reproduced well the observed data, confirming the dominant role of space charge effects in these detectors [5].

Although timing RPCs have so far been built with relatively small active areas per electronic readout channel (on the order of 10 cm^2), and are compatible with the high-multiplicity requirements of High-Energy Heavy Ion Physics, there is a number of possible applications in lower multiplicity environments ([6], [7]) for more coarsely segmented counters.

Having in mind such applications, in this paper we describe the structure and performance of a large counter, with an active area of 160×10 cm^2, readout by only 2 or 4 electronic channels.

* Corresponding author: Paulo Fonte, LIP - Coimbra, Departamento de Física da Universidade de Coimbra, 3004-516 Coimbra, PORTUGAL.
tel: (+351) 239 833 465, fax: (+351) 239 822 358, email: fonte@lipc.fis.uc.pt

2 Detector Description

The detector consisted of 3-mm thick float-glass plates with an area of 160×12 cm^2, and a measured bulk resistivity of 2×10^{12} Ω cm. The stack of plates, with attached copper foil[1] electrode strips (see Fig. 1), was mounted on a supporting 1-cm thick acrylic plate. Controlled pressure was applied to the stack by means of regularly spaced spring-loaded plastic bars. Four gas gaps were defined by glass fibers of 0.3 mm diameter, placed between the glass plates located beneath the pressing bars.

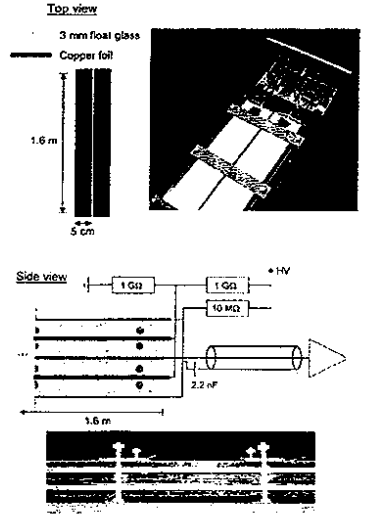

Figure 1: Pictures and schematic drawings of the detector.

Six individual electrode strips, with dimensions of 160×5 cm^2, were connected in two independent multi layer groups with a 1-mm wide pitch. The arrangement defined an active area of 160×10 cm^2, leaving uncovered a 1-cm wide region on the outer rim of the glass plates.

The ends of each group were connected via a short 50 Ω coaxial cable (see Fig. 1) to preamplifiers placed inside the gas volume, whose signal was fed through gas tight connectors to external amplifier-discriminator boards. The front-end chain was custom-made from commercially available analogue and digital integrated circuits, yielding measured timing and charge resolutions of 10 ps σ and 3.2 fC σ, respectively [8]. For stability reasons, the discriminators had a built-in dead time of 1 μs after each detected pulse contributing to the overall counter inefficiency.

High voltage of -6 kV was applied to the outer strips via 10 MΩ resistors and the signal traveling in these strips was fed to the shielding of the signal cables via 2.2 nF high-voltage capacitors (see Fig. 1). The central wire of the signal cables was connected directly to the central strips and to the preamplifier's inputs. To avoid the use of floating electrodes the glass plates, placed in the middle of each (upper and lower) half of the detector, had thin copper electrodes glued along their lateral edges, and were kept by a resistive voltage divider at half of the voltage applied to the outer strips.

[1] 3M conductive-adhesive copper tape.

The detector, high voltage distribution network, and preamplifiers were placed inside a gas-tight aluminium enclosure that was kept under a continuous flow of a nonflammable gas mixture consisting of 85% $C_2H_2F_4$[†] + 10% SF_6 + 5% iso-C_4H_{10} [9], at a flow rate close to 100 cm^3/min.

3 Test Setup and Data Acquisition

The tests were performed at the CERN PS using a secondary beam (T11) at 3.5 GeV, with mainly negative pions, during August 2000 run. The spills were 0.3 s long and spaced by a few seconds apart. Most tests were done with a defocused beam that illuminated the detector over a region of a few hundred cm^2.

A pair of plastic scintillation counters (Bicron BC420) measuring 8×3×2 cm^3 and readout on each face 3×2 cm^2 by a fast photomultiplier (Hamamatsu H6533) provided the reference time information. Both counters had a timing resolution close to 35 ps (σ) and a defined coincidence (trigger) area of 2×2 cm^2, placed upstream from the RPC.

The data acquisition system, based on the CAMAC standard, was triggered by the coincidence of both timing and scintillation counters.

After obtaining a valid trigger, the four timing signals from the reference scintillation counters and the RPC were digitized by a LeCroy 2229 TDC. A LeCroy 2249W ADC, operated with a gate of 300 ns, digitized the corresponding charge information. The TDC was calibrated using an Ortec 240 time calibrator and the ADC was calibrated by injecting in the preamplifiers a known amount of charge via the test inputs.

4 Data Analysis

Prior to any analysis, the TDC digitization error was taken into account by adding to each data value a random number distributed in the interval [-0.5, 0.5], and the events were selected by external and internal cuts.

After data cuts were obtained, the events were attributed to the strip showing the largest charge signal; the data from each strip was analyzed separately.

4.1 External Cuts

To clear the data from beam-related artefacts, i.e., multi particle events or scattered particles, several cuts were made based on the information collected from the timing scintillators. The events selected for further analysis had to comply with the following requirements:

- the difference between the TOF information from the timing scintillators (time average between both ends of a counter) should agree within ±2σ of the mean value;
- the position information from each timing scintillator (time difference between both ends of a counter) should be within ±2σ of the respective mean value[2];
- the charge measured on each timing scintillator should lie between the 5% and the 95% percentiles of the respective (strongly non-Gaussian) distribution.

All these distributions show wide tails beyond the specified cuts, which in turn generates corresponding tails in the time response of the RPC (see Sction 4.5).

Typically, about 50% of the events were accepted for analysis after external cuts were made.

4.2 Internal Cuts

The time difference between both strip ends (independent of the details of the avalanche development process and dependent only on its position) shows large bilateral tails that were cut at ±2σ of the mean value[3]. This cut had a negligible effect on the time resolution of the counter, but it strongly reduced the amount of timing tails close to the strip ends (see Section 4.5). Tighter cuts have less influence and presumably the remaining timing tails are mostly due to the physical processes related to the onset and development of the avalanche (depending, for instance, on applied voltage - see Section 5.4).

It should be noted that when the quality of the trigger was enhanced by requiring an additional coincidence with a small (0.3×0.6 cm^2) scintillator placed downstream from the RPC, the amount of tails became negligible (see Figure 8) and the cut mentioned above had little effect on the results, suggesting that the need for such a cut arises mainly due to beam quality limitations.

For an accurate correction of the measured time as a function of charge and to decrease the amount of timing tails seen by the RPC without significant efficiency loss, a 1% cut was made in the lower part of the RPC charge distribution (see Fig. 2). (The RPC charge was defined as the sum of the charges sensed on both ends of each strip.)

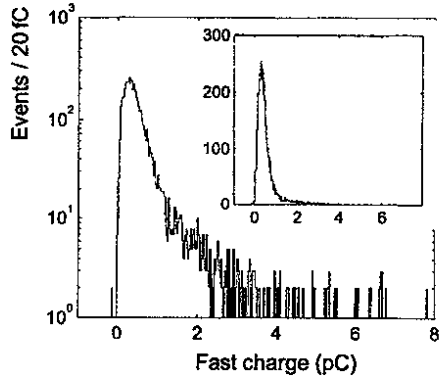

Figure 2: Typical fast charge[4] distribution in logarithmic and linear (inset) scales.

4.3 Detection Efficiency

The detection efficiency for each strip was determined after the external cuts and before the internal cuts were made. The impact of the (optional) internal cuts should be subtracted from the efficiency values given in all figures.

Two different definitions of detection efficiency were formed by the ratio of the following quantities to the total number of events:

- the number of events yielding an amount of charge in the RPC larger than the upper limit of the ADC pedestal distribution (charge efficiency);
- the number of events for which valid time was measured in the RPC (time efficiency).

In principle, both definitions should yield similar results except if a considerable amount of inter-strip crosstalk will be present. In this case the crosstalk signal, not being galvanically coupled, will not contribute to any net charge but may induce a voltage level above the discriminating threshold, generating a valid-time event.

4.4 Position Accuracy

A position-dependent timing information can be formed for each event by the time difference between both strip ends. This information was calibrated with respect to a known displacement of the RPC and it was charge-corrected in a manner similar to the TOF information (Section 4.5).

[†] Commercially known as R134a.

[2] The position spread was mainly related to the width of the 2×2 cm^2 coincidence-selected trigger region.

[3] Note that the same type of cut was applied to the timing scintillator data.

[4] Electronic component of the signal.

4.5 Timing Accuracy

In principle, position-independent timing (TOF) information can be formed for each event by averaging the time measured on both strip ends. However, it was found that close to the extremes of the counter, the TOF information was correlated with the position information and a linear correction could be applied to the former as a function of the later. Data will be presented with and without this position correction.

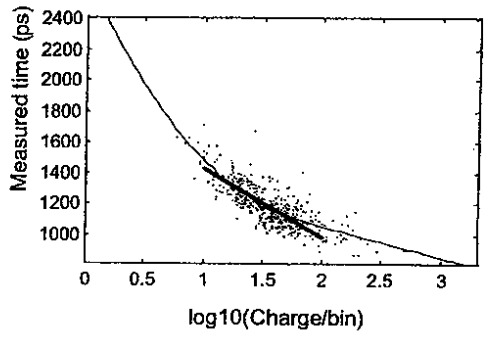

Figure 3: Typical time vs. log (charge) correlation plot, showing the calculated time-charge correction curve (thin line) and the average slope (thick line).

The TOF information strongly correlates (see Fig. 3) also with the measured signal charge and the correction was made along the lines described in Ref. [2]. The method automatically determines and corrects the contribution of the reference counters time jitter.

The resulting time distribution was not purely Gaussian, showing a bilateral excess of events (timing tails) exemplified in Figure 4. We opted to separately characterize the main timing resolution figure (σ) and the amount of timing tails, since the later can, or cannot, be important, depending on the application.

The main resolution figure was determined by a Gaussian fit to the corrected time distribution (with 5 ps bins) within $\pm 1.5\ \sigma$ of the mean value, and the timing tails were characterized as the fraction of events whose distance to the mean value exceeds 300 ps. For a purely Gaussian distribution with $\sigma \leq 100$ ps, the fraction should be smaller than 0.3%.

For each run the time vs. log (charge) correlation curve, which is almost linear, was characterized by the average time, charge, and slope (see Fig. 3). This information was used to assess the stability of the time-charge correlation and the need for separate correction curves at different positions along the counter.

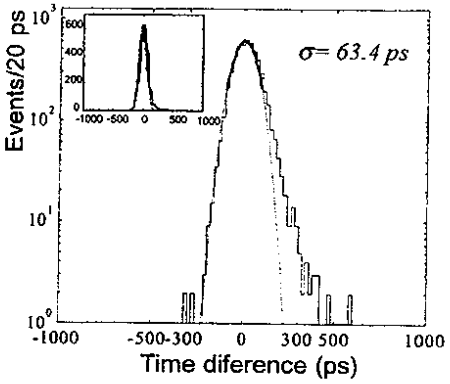

Figure 4: Typical time distribution (from strip B at X = -30 cm) after charge correction in logarithmic and linear (inset) scales. The thick line corresponds to a Gaussian curve fitted within $\pm 1.5\ \sigma$ to determine the main resolution figure (after correction for the contribution of the start counters (see Section 4.5) the timing resolution for this example is σ_t=53 ps). The dashed line corresponds to the extension of the fitted Gaussian to $\pm 3.5\ \sigma$. Timing tails were defined as the fraction of events whose absolute time deviation from the average was larger than 300 ps, which amount in this example to 0.4 %.

5 Results and Discussion

In the following discussion, we will refer to the position of the center of the trigger region along and across the strips as, respectively, the X and Y coordinates, defining the origin of the coordinate system in the geometrical center of the counter.

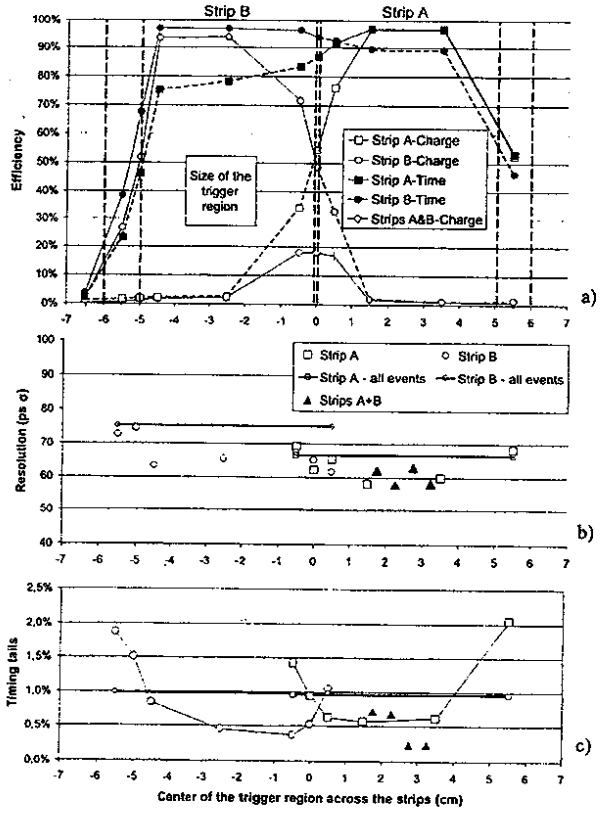

Figure 5: Several quantities of interest as a function of the position of the center of the trigger region across the strips. a) Charge and time efficiency. The lower curve corresponds to the fraction of events that show a measurable amount of charge in both strips. The superimposed dashed lines indicate the position of the copper strips, and the outer dotted lines indicate the edge of the glass plates. b) Timing resolution with a separate analysis in each position and when all events for each strip are analysed simultaneously. The solid triangles correspond to data taken with both strips connected together. c) Same as b), for the timing tails.

5.1 Detection Efficiency and Crosstalk

Charge and time efficiency curves as a function of Y (for X=0) are shown in Fig. 5a. The fraction of events inducing a measurable amount of charge in both strips is also shown, probably corresponding to avalanches occurring close to the inter-strip region.

When the trigger region was fully contained within a single strip, the charge and time efficiencies closely match for that strip, while the opposing strip shows very reduced charge efficiency and a considerable (from 80% to 90%) time

efficiency. This large crosstalk level (see Section 4.3), actually to be expected on such long strips, did not significantly affect the timing characteristics of the device, but would affect its multi hit capability.

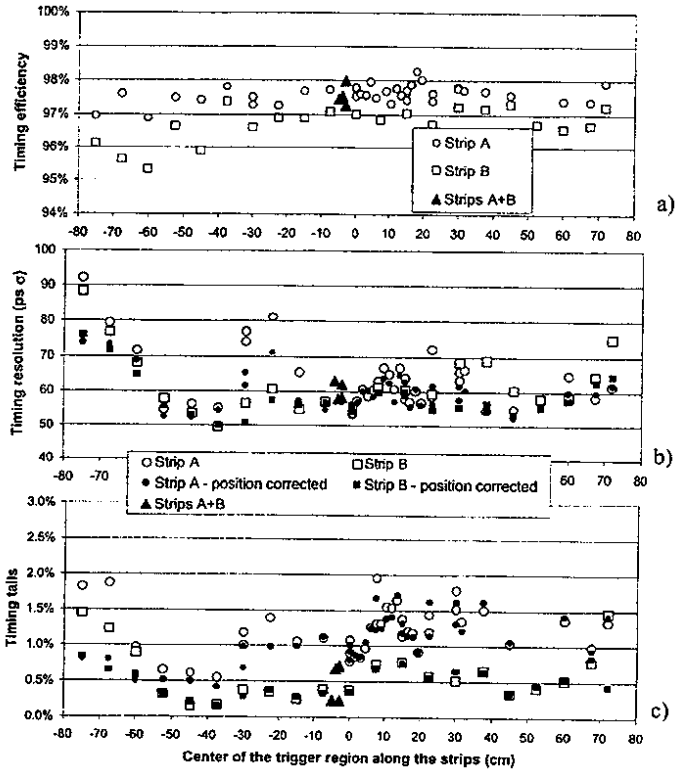

Figure 6: Several quantities of interest as a function of the position of the center of the trigger region along the strips. a) Time efficiency, better than 95%; b) Time resolution with and without position correction, ranging from 50 to 90 ps σ (50 to 75 ps σ with position-dependent time correction). c) Timing tails with and without position correction, smaller than 2%. In all figures, the solid triangles correspond to data taken with both strips connected together.

In Fig. 6a the time efficiency is shown as a function of X (for Y = ±3 cm, corresponding essentially to the center of each strip). The measurements were generally taken in steps of 7.5 cm except for a region of strip A, between 0 and 20 cm, that was scanned in steps of 1.5 cm to assure that at least one measurement contained a spacer.

The values range between 95% and 98%, being slightly larger for strip A. This small difference can be attributed to slight differences in the gain of the front-end electronics chain. However, it should be noted that a smaller chamber of similar construction has shown a time efficiency above 99% [2]. The slightly reduced efficiency found in the present counter can be attributed to a poorer trigger quality, evidenced by the tails visible in the scintillators time and position

information (see Section 4.1), and to a much larger sensitive area that collects a larger event rate from the wide beam (see the discussion about the discriminators dead-time in Section 3).

The combination of both strip signals into a single amplifier for each end of the counter, doubling the active area per amplifier, caused absolutely no degradation in the detection efficiency. Also no influence from the spacers could be found in the fine-step scan.

5.2 Timing Accuracy

5.2.1 Timing Resolution

The timing resolution is shown as a function of Y (for X = 0) in Fig. 5b. It ranges from 58 to 76 ps (σ) across the counter, including both the outer edges and the inter-strip region. Since in a real application there would be no possibility to determine the avalanche position along Y, in the same figure we also present the resolution figure (horizontal lines) obtained by analysing a data set for each strip containing equal number of events from each position, yielding 67 to 76 ps (σ) for strips A and B, respectively.

In Figure 6b, we show the timing resolution as a function of X (for Y = ±3 cm). Most data points range from 50 to 70 ps σ, except for two regions, around -20 cm and -70 cm, where the resolution was degraded to 80 and 90 ps σ, respectively. This degradation most probably has a local mechanical origin, since it is not symmetrical with the counter geometry and are not identical for both strips.

The combination of both strip signals into a single amplifier for each end of the detector, doubling the active area per amplifier, caused absolutely no degradation in the time resolution of the device. Also no clear influence from the spacers could be found in the fine-step scan.

5.2.2 Timing Tails

The magnitude of the timing tails is shown as a function of Y (for X = 0) in Fig. 5c. The tails do not exceed 2% of the total number of events, being smaller than 1% in the center of the strips. The effect is larger in the outer edges than in the inner strip edges, possibly because no attempt was made to sharply reduce the electric field at the strip edges (the glass plates extend up to 1 cm, beyond the copper strips). Avalanches occurring in this space will induce currents, both in the strips and in the enclosing gas box, creating a position-dependent induced charge fluctuation that may cause timing errors. A similar phenomenon can be perceived in the space between the strips, where the induced charge was shared among the strips in a position-dependent manner (see also Fig. 5a).

In Fig. 5c, we also present the values obtained by analyzing for each strip a data set (horizontal lines) containing an equal number of events from each position, yielding tails of 1% for both strips.

In Fig. 5c, we show the amount of timing tails as a function of X (for Y = ±3 cm). Strip B shows tails generally below 1.0%, raising up to 1.5% close to the counter extremities. Strip A shows larger tails, up to 2% over the whole counter. A possible reason for this difference, that doesn't appear in the Y-scan (Fig. 5c), could be a momentary beam quality fluctuation.

The combination of both strip signals into a single amplifier for each side of the detector, doubling the active area per amplifier, caused absolutely no degradation in the amount of tails and no clear influence from the spacers could be found in the fine-step scan.

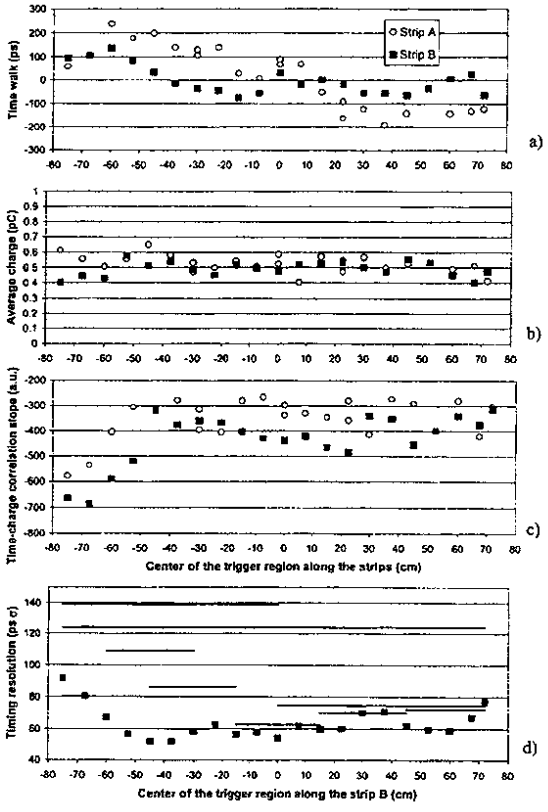

Figure 7: Several quantities related to the time-charge correlation curve (see Figure 3) are plotted as a function of the position of the trigger region along the strips[5]. a) Variations of the average measured time, covering a range of 400 ps. b) Average measured charge, which shows little variation along the counter. c) The average slope shows considerable variations along the counter, particularly an the left-hand side, where a poorer time resolution is also visible (see Figure 6). d) Joint analysis of a data set containing an equal number events from each of the positions indicated by the extent of the horizontal lines: the right-hand side is only weakly affected by position dependent effects, while the left-hand side would require a more finely segmented calibration procedure.

[5] It should be stressed that these variations can be corrected by calibration, using the position information given by the time difference between both strip ends (Fig. 8).

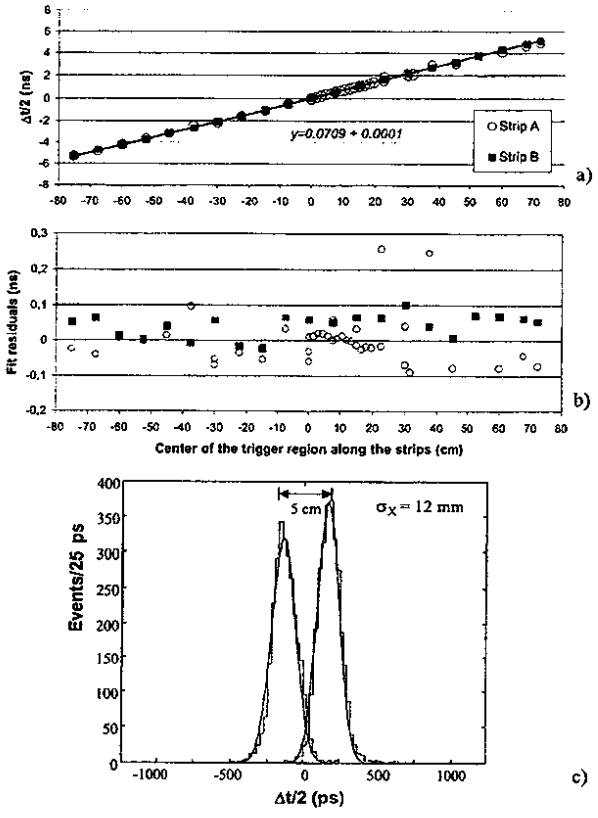

Figure 8: a) Time difference between both strip ends, as a function of the position of the trigger region along the strips. There is an accurately linear dependency (evidenced by the small residues shown in b)), with a slope of 70.9 ps/cm, corresponding to a signal propagation velocity of 14.1 cm/ns. c) The width of the trigger region was reduced to 3 mm in the X direction, and the spread of the time difference was compared with a measured displacement of 5.0 cm, yielding a position accuracy of 12 mm σ.

5.2.3 Variations of the Measured Time and Charge Along the Counter

Due to mechanical or electrical inhomogeneities, position dependent charge and time variations along the counter are expected. This effect should be corrected by calibration, using the counter's position resolution (discussed in Section 4.4).

In Fig. 7, we show the variations of time (a), charge (b) and of the slope of time vs. the log(charge) correlation curve (c), represented in Fig. 3, as a function of X (for Y = ±3 cm). Variations of the average time by about 400 ps are apparent along with large changes of the time vs. log(charge) correlation slope, while the average charge remains

relatively stable. It should be noted that the large slope variations visible in the left-hand side of Fig. 7c correlate well with the degradation of the time resolution visible in the same region of Fig. 6b.

To directly evaluate the influence of these position dependencies on the time resolution of the counter as a function of the segmentation of the calibration procedure along X, we have combined an equal number of events from adjacent positions along strip B and analysed jointly the resulting data set. The results are shown in Fig. 7d: events from the right-hand side of the counter could be jointly analysed without much degradation arising from position dependent effects, while the left-hand side was severely affected by such effects, calling for a finer segmentation of the calibration procedure. Such features have probably a local mechanical origin, since all other variables are equal along the counter.

5.3 Position Resolution

In Fig. 8a, the time difference between both strip ends is plotted as a function of X (for Y = ±3 cm) showing an accurately linear dependency with a slope of 70.9 ps/cm, which corresponds to a signal propagation velocity of 14.1 cm/ns. In Fig. 8b, the time difference distribution is plotted for two trigger positions 5.0 cm apart, yielding a position accuracy of 12 mm σ. For this measurement, the width of the trigger region in the X direction was reduced to 3 mm via an extra coincidence scintillator.

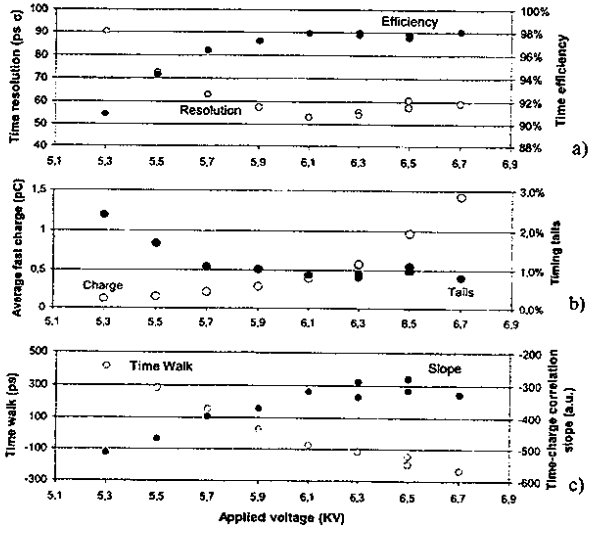

Figure 9: Several quantities of interest plotted as a function of the applied voltage. a) Time resolution and efficiency. b) Average amount of fast charge and the amount of timing tails. c) The variation of the absolute value of the measured time and the slope of the time vs. log(charge) correlation curve.

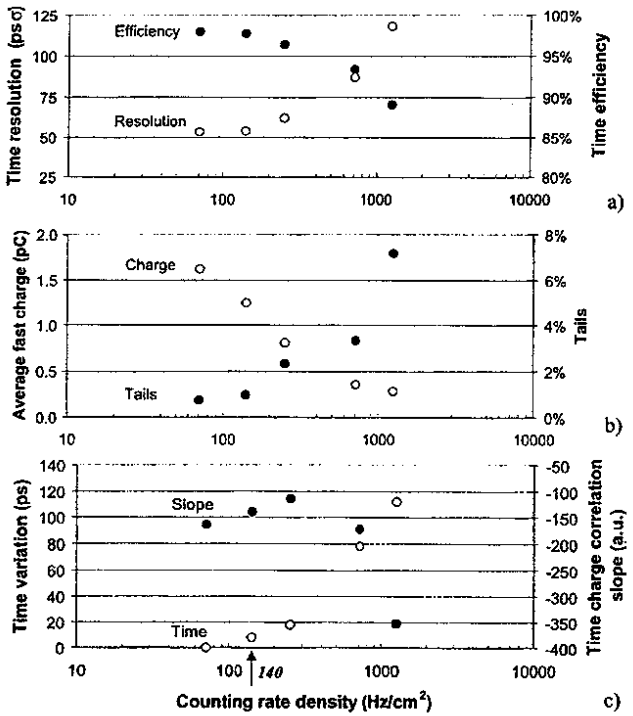

Figure 10: Several quantities of interest plotted as a function of the counting rate density. a) Time resolution and efficiency. b) Average fast charge and amount of timing tails. c) The variation of the absolute value of the measured time and the slope of the time vs. log(charge) correlation curve. The vertical arrow indicates the counting rate at which most of the measurements were taken.

5.4 Behavior as a Function of the Applied Voltage

It is interesting to study how some of the quantities mentioned above change as a function of the applied voltage, as illustrated in Fig. 9.

Figure 9a shows the evolution of the time resolution and efficiency, the later showing a plateau of 98% above 6.1 kV, while the former shows a broad minimum at 52 ps σ close to 6.1 kV. This voltage has been chosen as the optimum operating point and most of the data presented in the previous sections has been taken at this setting.

Figure 9b shows the evolution of the average fast charge and of the amount of timing tails. The behavior of charge as a function of voltage was already discussed at length in Ref. [4], and we will not further elaborate on this subject here. The amount of timing tails decreases with increasing voltage and reaches a plateau of 1% above 5.9 kV.

Figure 9c shows the variation of the absolute measured time and of the time vs. log(charge) correlation slope. As expected, the measured time shows a negative variation, compatible with a larger value of the avalanches exponential growth parameter; further details on this subject can be found in Refs. 4,5, and 8. The time vs. log(charge) correlation slope becomes less steep with increasing voltage, reaching a plateau above 6.3 kV.

5.5 Behavior as a Function of the Counting Rate

Being that the counting rate capability is an important characteristic of RPCs, several quantities of interest were studied as a function of rate per unit area, see Fig. 10. The vertical arrow indicates the standard operating point (140 Hz/cm²) at which most of the measurements presented here were taken.

Figure 10a shows the variation of the time resolution and efficiency. Both quantities are constant below 140 Hz/cm², and degraded at larger counting rates. Operation up to 500 Hz/cm² may be possible if a slight degradation of the counter performance is accepted (comparable with the performance variations observed as a function of position).

Figure 10b shows the evolution of the average fast charge and the amount of timing tails. The average fast charge shows a continuous decrease with the increasing counting rate, suggesting a counting-rate induced reduction of the average electric field in the amplifying gap, while the timing tails remain quite small (less than 4 %) up to 1 kHz/cm².

Figure 10c shows the variation of the absolute measured time and of the time vs. log(charge) correlation slope. The average measured time shows a positive variation, compatible with the observed reduction of the gas gain, which is nevertheless quite small (±10 ps) around the standard operating point, while the slope remains essentially unchanged around this point. It should be stressed that any variations of these quantities can be taken into account by appropriate calibration.

The general behavior of the detector characteristics as a function of the counting rate indicates that there is no degradation of the performance up to 140 Hz/cm², and a counting rate of 500 Hz/cm² could be handled if a slight performance degradation will be acceptable.

Conclusions

We built and tested a large area timing RPC, with an active surface of 160×10 cm², to be applied in medium (e.g. Ref. [6]) or low multiplicity (e.g. Ref. [7]) TOF counters. The active area was segmented in two readout strips, each measuring 160×5 cm², sensed in both ends by identical custom-made, very high-frequency, front-end electronic channels [8].

A timing resolution between 50 and 90 ps σ, with an efficiency between 95% and 98% for MIPs, was attained over the whole active area. The performance could be improved close to the strip ends by correcting the measured time as a function of the measured avalanche position, thus improving the time resolution range to lie between 50 and 75 ps σ.

The combination of both strip signals into a single amplifier for each end of the detector, doubling the active area per amplifier, caused absolutely no degradation in the efficiency or in the time resolution of the device. Also no clear influence from the spacers could be found in a fine-step scan.

The avalanche position along the counter could be determined from the time difference between both strip ends, yielding a position resolution of 1.2 cm σ along the strips with very good linearity.

Timing tails, defined as the fraction of events whose absolute time deviation from the average was larger than 300 ps, were smaller than 2%, occurring the larger values in the outer edges of the detector and close to the strip ends.

The general behaviour of the detector characteristics as a function of the counting rate indicates that there is no degradation of the performance up 140 Hz/cm², and that a counting rate of 500 Hz/cm² could be handled if a slight degradation is accepted.

Probably due to structural inhomogeneities, there were considerable variations of the average measured time along the counter, requiring a calibration procedure segmented every few tens of centimeters. In an experimental array, this segmentation would be achieved with the help of the counter's position resolution.

The large inter-strip crosstalk level observed (80%) does not seem to influence the time resolution of the counter, affecting only its multi-hit capability. It should be considered whether for a given application it is not preferable to base the detector on multiple layers of single-strip chambers, reaching full geometrical coverage and avoiding any cross-talk. A multilayer configuration, providing multiple measurements for each particle, would also have the advantages of being self-calibrating and allow an improved rejection of timing tails

Acknowledgements

We are grateful to Paolo Martinengo and Piotr Szimanski of the ALICE test beam support team for their efficient and friendly cooperation. We thank Juan Garzon from the University of Santiago de Compostela for his interest and

support. We are grateful to José Pinhão, Américo Pereira, and Fernando Ribeiro from our technical staff for their competent collaboration.

This work was done in the framework of the FCT project CERN/P/FIS/15198/1999.

References

[1] P. Fonte, A. Smirnitski, and M.C.S. Williams, "A New High-Resolution Time-of-Flight Technology," *Nucl. Instr. and Meth. in Phys. Res. A*, 443 (2000) 201.

[2] P. Fonte, R. Ferreira Marques, J. Pinhão, N. Carolino, and A. Policarpo "High-Resolution RPCs for Large TOF Systems," *Nucl. Instr. and Meth. in Phys. Res. A*, 449 (2000) 295.

[3] A. Akindinov et al., "A Four-Gap Glass-RPC Time of Flight Array with 90 ps Time Resolution," ALICE note ALICE-PUB-99-34, preprint CERN-EP-99-166.

[4] P. Fonte and V. Peskov. "High-Resolution TOF with RPCs", presented at the "PSD99 - 5th International Conference on Position-Sensitive Detectors," 13-17 th September 1999, University College, London, preprint LIP/00-04 http://xxx.lanl.gov/abs/physics/0103057.

[5] P. Fonte, "High-Resolution Timing of MIPs with RPCs – a Model," presented at the "RPC99 - 5th International Workshop on Resistive Plate Chambers," 28 - 29th October 1999, Bari, Italy, *Nucl. Instr. and Meth. in Phys. Res. A*, 456 (2000) 6.

[6] FOPI-Collaboration, "Upgrading the FOPI Detector System," *GSI-Scientific Report*, (1998), pp. 177.

[7] The HARP collaboration (PS214), "The Hadron Production Experiment at the PS," CERN-SPSC/99-35, SPSC/P315, 15 November, 1999.

[8] A. Blanco, N. Carolino, P. Fonte, and A. Gobbi, "A Simplified and Accurate Front-End Electronics Chain for Timing RPCs," presented at the "LEB 2000-6th Workshop on Electronics for LHC Experiments", 11-15 September 2000, Cracow, Poland, published in the conference proceedings CERN 2000-010 CERN/LHCC/2000-041.
A. Blanco, N. Carolino, P. Fonte, A. Gobbi, "A New Front-End Electronics Chain for Timing RPCs", presented at the "2000 IEEE Nuclear Science Symposium and Medical Imaging Conference", 15-20 October 2000, Lyon, France, accepted for publication in *IEEE Trans. Nucl. Sci.*

[9] P. Camarri et al, "Streamer suppression with SF_6 in RPCs operated in avalanche mode, "*Nucl. Instr. and Meth. in Phys. Res. A* 414 (1998) 317.

Applications and New Developments in Resistive Plate Chambers

P. Fonte

ISEC and LIP, Coimbra University, Coimbra P-3000, Portugal (e-mail: fonte@lipc.fis.uc.pt).

Abstract

Resistive Plate Chambers are rugged and affordable gas detectors that have found extensive use in high-energy physics and astroparticle experiments. The main features of these counters are the very large pulse height, reduced cost per unit area and good (about 1ns) time resolution.

The field has enjoyed very active progress in recent years, including the introduction of a new (avalanche) mode of operation, extension of the counting rate capabilities to levels around 10 MHz/cm^2, improvement of the time resolution for MIPs to 50 ps σ, and the achievement of position resolutions of a few tens of μm.

These new developments have expanded the range of HEP applications and promise new applications in medical imaging.

I. INTRODUCTION

Resistive Plate Counters (RPCs) were introduced in 1981 [1] as a practical alternative to the remarkable "localized discharge spark counters" [2], which ultimately achieved a time resolution of 25ps σ [3]. The resulting detector, being by construction free from damaging discharges and enjoying a time resolution of the order of 1ns, has found very good acceptance in high-energy and astroparticle physics.

In modern language, the original RPCs were single gap counters operated in streamer mode. Soon, the double gap structure was introduced [4] to improve the detection efficiency along with the avalanche mode of operation [5], which extends its counting rate capabilities.

An imaginative construction method, denominated "multigap RPC" was introduced in 1996 [6], being specially suited for the construction of counters with more than a single gas gap.

Recent innovations in detector construction and readout electronics have extended the timing resolution of RPCs for minimum ionizing particles (MIPs) to 50 ps σ [7], the rate capability to 10^5 Hz/mm^2 [8] and the position resolution for X-rays to 30 μm FWHM in digital readout mode [9].

Single and double gap, streamer-mode RPCs have so far found application in cosmic ray experiments, like COVER_PLASTEX [10] and EAS-TOP [11] being also used in the high-energy physics experiments L3 at CERN, BABAR at SLAC, USA, and BELLE at KEK, Japan. Future applications will include the ARGO experiment at the "YangBaJing High-altitude Cosmic Ray Laboratory" [12], and the OPERA [13], and MONOLITH [14] cosmic ray experiments in LNGS, Italy. The Muon Arm of the ALICE experiment at LHC [15] will also be equipped with streamer-mode RPCs. Avalanche-mode RPCs will be used for the muon trigger systems of the ATLAS [16], CMS [17], and LHCb [18] experiments at LHC.

Timing RPCs, a recent development [19], are already in use by the HARP experiment at the CERN PS accelerator [20] and will equip the 160 m^2 TOF barrel of ALICE's Particle Identification Detector [21].

II. RPC DESIGNS

The combination of resistive and metallic electrodes with signal-transparent semi-conductive layers, highly isolating layers, and different kinds of pickup electrodes endows the RPCs with a rich variety of configurations, tunable to a variety of requirements.

This work was supported by Fundação para a Ciência e Tecnologia in the framework of the project CERN/P/FIS/40111/2000.

A. Single Gap

The original RPC design [1], included a single gas gap delimited by Bakelite resistive electrodes. Naturally, the counter design has evolved since then, and a modern example is shown in Fig. 1.

The application of the polarizing potential to the resistive electrode via an electrode with a lower resistivity, but still transparent to the induced signals (see for instance Refs. [22] and [23]) allows us to operate both signal pickup electrodes at ground potential, while saving the utilization of high-voltage capacitors and avoiding the need for high voltage insulation of the strips.

Glass electrodes, enjoying a mechanical stiffness and surface quality much superior to bakelite, have also been considered in the past and remain in use today (see for example Refs. [2], [24], and [25]).

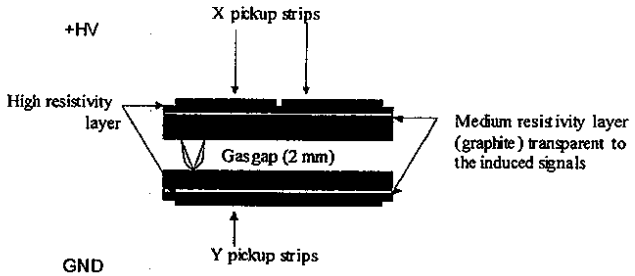

Fig. 1. Schematic drawing of the single-gap streamer mode RPC used by the BABAR experiment [52].

B. Double Gap

Double gap designs [4] having a larger number of elements (gas gaps, pickup electrodes), allow for more varied structures than the single gap ones, and two such designs are presented as examples in Fig. 2.

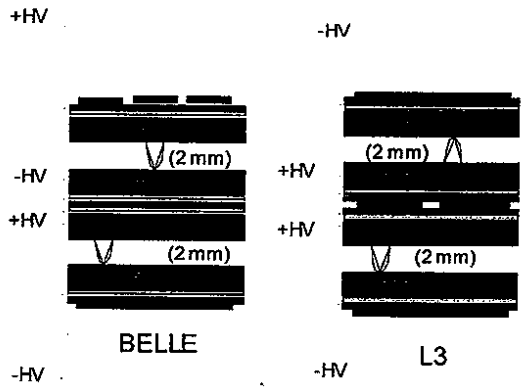

Fig. 2. Schematic drawing of the double-gap RPCs used by the L3 [69] and Belle [53] experiments.

C. "Multigap"

A construction method denominated "multigap RPC" was introduced in 1996 [6], being especially well-suited for the construction of counters with more than a single gas gap. A schematic drawing is shown in Fig. 3.

The most preeminent feature of this design is the inclusion of resistive, electrically floating electrodes that divide the gas volume into a number of individual gas gaps, without the need of any conductive electrodes. According to its inventors the steady-state requirement for a null total current on each of the dividing electrodes stabilizes their potential at a value that equalizes the currents flowing in and out by adjusting the gas gain in the neighboring gaps.

Possible drawbacks of this design are the large voltages required, and the fact that at low ionizing particle fluxes the stabilizing mechanism may be dominated by the dark counting rate.

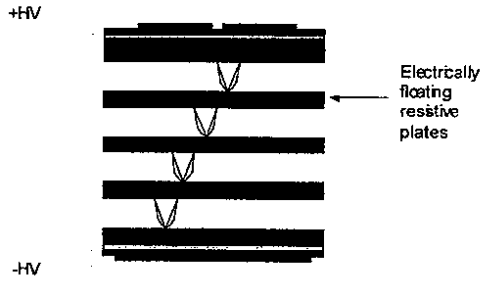

Fig. 3. Schematic drawing of the "multigap" RPC [6].

D. Hybrid Designs

Metallic and resistive electrodes may be combined and still retain the main property of the RPC: the total absence of violent discharges. The only requirement is that no gas gap will be delimited by two metallic electrodes.

Actually, the gas counter formed by two parallel metallic electrodes defining a gas gap is denominated Parallel Plate Chamber (PPC), which has found wide application in the detection of heavy ions and, with wire-mesh electrodes, proposed long ago for high-rate applications [26]. However, possibly due to the violent nature of the discharges, this type of counter never found wide acceptance in HEP.

A few schematic examples of hybrid RPCs can be seen in Fig. 4.

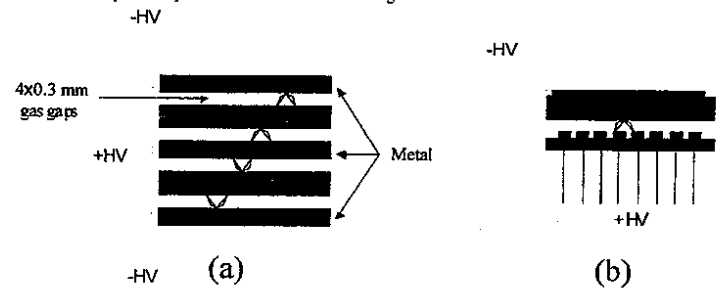

Fig. 4. Examples of hybrid (metallic+resistive electrodes) RPC constructions. a) a four-gap counter used for timing [7], and b) microRPC [9].

IV. Modes of Operation

A. Nature of the Operation Modes

RPCs may be operated in avalanche mode or discharge mode.

The avalanche mode corresponds to the generation in the gas gap of a Townsend avalanche, following the release of primary charge by the incoming ionizing radiation.

In discharge mode, the avalanche is followed by a "streamer" discharge [27]. In a metallic counter, the discharge will evolve via a sequence of avalanche, streamer, glow discharge, filamentary discharge, and spark [28]. However, the later discharge stages require a considerable current, up to few Amperes, to flow in the gap which is forbidden by the high resistivity of the RPC electrodes.

Optical observations suggest that in glass, the RPCs discharge is quenched at the filamentary discharge stage ([29], [30]). However, for electrode resistivities of the order of 4×10^{7} Ω-cm, a permanent glow discharge could sometimes be observed [8].

B. Space Charge Effect

The space charge present in a Townsend avalanche creates its own electric field that is summed to the applied electric field. Three regions can be identified: the total field is larger than the applied field, immediately upstream and downstream from the avalanche, and lower than the applied field over the main avalanche body [31]. For avalanches approaching 10^{8} electrons (the Raether limit [27]), the high-field regions generate the conditions for the development of the cathode and anode (backward and forward) streamers, while the lower field region causes the reduction of gas gain seen by the avalanche (avalanche saturation effect) [27]. Both phenomena, avalanche saturation and streamers, share a common physical origin and are normally simultaneously present.

The existence of a strong avalanche saturation effect in RPCs has been experimentally verified, and has been shown to play a central role in the interpretation of the charge spectra and efficiency characteristics, both for millimeter scale ([32], [33]) and sub-millimeteter scale ([34], [35]) gas gaps.

C. Available Signal

The charge signal ranges from a few pC for the fast (electron) component of the signal in avalanche mode to a range between 50 pC [36] and a few nC ([37] for instance) in streamer mode.

Naturally, due to the high resistivity of the electrodes, there is a tradeoff between the available signal charge and the counting rate capability (see section V).

D. Gas Mixtures

Modern standard RPCs working in avalanche mode use mostly mixtures of tetrafluoroethane ($C_2H_2F_4$) with 2 to 5% of isobutane (iso- C_4H_{10}) and 0.4% to 10% of sulphur hexafluoride (SF_6). The addition of SF_6 has been shown to extend the streamer-free operation region, and to reduce the amount of charge in the streamer ([32], [38]).

In streamer mode, mixtures of argon with isobutane and tetrafluoroethane in widely varying proportions tend to be used.

It was recently shown that the addition of SF_6 (4%) to the remaining constituents allowed to reduce the streamer charge to 50 pC, and extend the counting rate capability to 300 Hz/cm² while keeping an efficient streamer-mode operation [36].

V. Efficiency for MIPs

In Fig. 5, a survey of recently published results concerning the efficiency of RPCs for MIPs is shown. For the sake of comparison the reported efficiency of multiple-gap chambers was converted to efficiency per gap ($\varepsilon_{(1gap)}$) figure by using the formula

$$\varepsilon_{(1\,gap)} = 1-\bar{\varepsilon}_{(1\,gap)} \approx 1-\sqrt[n]{(1-\bar{\varepsilon}_{(n\,gap)})} \qquad (1)$$

which considers the gas gaps as approximately independent counters.

It can be seen that most standard 2-mm gap RPCs show per gap efficiencies between 85% and 95%, irrespective of the operation mode. Smaller gap RPCs show a somewhat reduced efficiency; however, it's still surprisingly large (45%) for 0.1 mm gaps. The difficulties arising with the interpretation of such data have been addressed in Ref. [35].

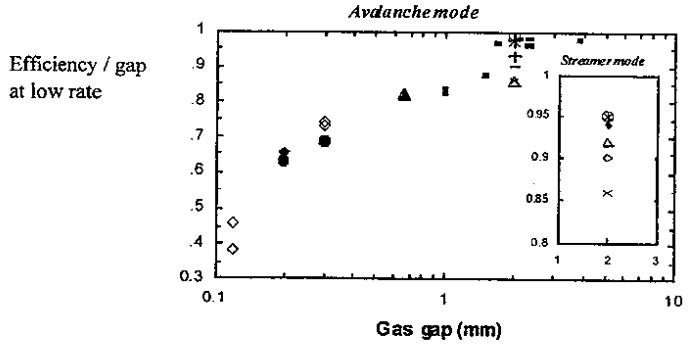

Fig. 5. Survey of recently published results concerning the per gap efficiency of RPCs for MIPs (see the text for calculation details) as a function of the gap width. The efficiency decreases from 85 to 95% per gap with 2-mm gaps, irrespective of the operation mode to 45% with 0.1 mm gaps in avalanche mode. (Main figure: closed square [58], open square [63], closed diamond [45], open diamond [34], ˙ [62], + [61], X [65], * [60], closed circle [7], open circle [59], closed triangle [39], open triangle [64]. Inset: open square [57], closed diamond [67], open diamond [36], X [43], * [52], open circle [66], open triangle [53])

VI. Rate Capability

A. Standard RPCs

In Fig. 6 a survey of recently published results concerning the counting rate capability of modern RPCs is presented as a function of the resistivity of the electrodes.

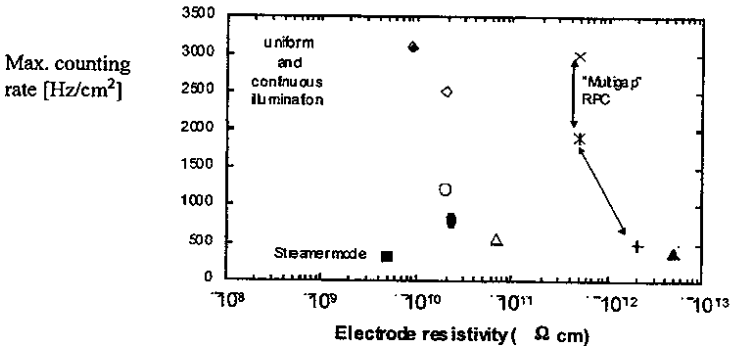

Fig. 6. Survey of recently published results concerning the counting rate capability of standard RPCs as a function of the resistivity of the electrodes. Only measurements taken with uniform and continuous illumination were considered. Present state-of –the-art counters reach 3 kHz/cm² in avalanche mode and 300 Hz/cm² in streamer mode. Special devices reach much higher rates (Fig. 7). (Legend: closed square [36], closed diamond [59], open diamond [60], X [68], * [62], + [45], open circle [62], closed circle [64], open trangle [63], closed triangle [65])

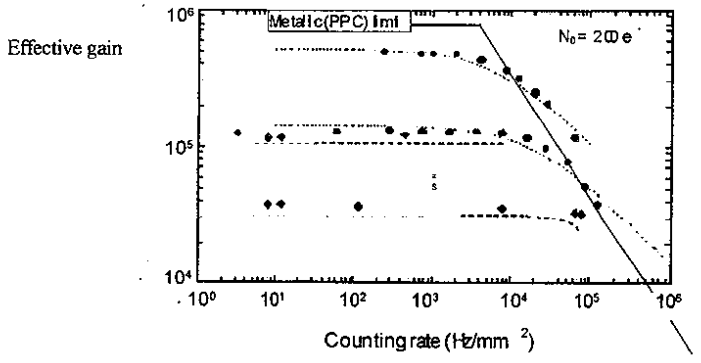

Fig. 7. Effective gas gain as a function of the counting rate for some special RPCs: PPAC with low resistivity anode [8] (closed circle) and MicroRPC (closed diamonds) [35] (see also Fig. 4). The solid line indicates the intrinsic counting rate limitation of metallic counters ([40],[42]),which is reached by both devices.

Only measurements taken with uniform and continuous illumination were considered. An over-optimistic estimation of the rate capabilities may arise if only a small area is irradiated (due to lateral currents in the electrodes), or if pulsed beams are used (see for instance [39]), presumably due to capacitive and electrode polarization effects. The maximum counting rate corresponds typically to a reduction in the counter efficiency by a few percent.

Present state-of-the-art standard high-rate RPCs reach 3 kHz/cm^2 in avalanche mode and 300 Hz/cm^2 in streamer mode. The data for the "multigap" RPC forms a different curve, seeming to offer an advantage in terms of counting rate capability for a given electrode resistivity.

B. Special RPCs

The combination of typical metallic counter structures like PPC or PPAC [26] with appropriated resistive electrodes yields discharge-tolerant counters that can reach very high counting rates.

In Fig. 7, the effective gas gain as a function of the counting rate is shown for some special RPCs. A PPAC with a low resistivity ($\rho = 4\times10^7\Omega$·cm) anode [8] and a microRPC (see also Fig. 4) with a Si cathode ($\rho = 10^4\Omega$·cm) and metallic anode ([40], [41]). Both devices reach the intrinsic counting rate limitation of metallic counters ([40], [42]), indicating that no further reduction of the electrode resistivity below $10^7\Omega$·cm is required for very high rate RPCs.

VII. Background Counting Rate

Due to the nature of the electrodes, RPCs can accommodate relatively large background (dark) counting rates without much adverse effects. However such currents, above limit, may affect the local and global rate capability, increase the occupancy of the readout electronics, and induce faster ageing.

In Table 1 the published dark count rates of several counters are listed along with their mode of operation, the electrode material, and gap widths. It seems that 2-mm gap streamer mode counters made of glass or bakelite often show dark counting rates on the order of 1 kHz/m^2. Thinner gap counters, like timing RPCs, show a larger dark counting rate, possibly on account of their much larger surface electric field.

These numbers should however be compared with the counting rate capabilities of standard RPCs reported in Section V(A), ranging from 3×10^3 kHz/m^2 to 3×10^4 kHz/m^2.

The 0.4 mm counter made with very clean Si electrodes stands out as featuring a very high counting rate along with a low dark rate for such a small gap.

It should be noted that many authors quote the dark currents instead of the dark count rate. Since the dark currents include an unknown fraction of conduction current through the spacers and frames, it is impossible to calculate which part corresponds to an effective counter occupancy.

The problem of understanding and reproducibly controlling the dark count rate of RPCs, is one of the most important open problems for practical applications.

TABLE 1

REPORTED DARK COUNT RATES OF SEVERAL COUNTERS ALONG WITH OTHER DATA OF POSSIBLE INTEREST FOR ITS INTERPRETATION

mode	material	gap width	rate capability (kHz/m^2)	Dark rate (kHz/m^2)	Ref.
avalanche	glass	0.3	3000	12.5	[46]
avalanche	melamine	0.66	19000	600	[39]
avalanche	Si	0.4	10^8	1.6	[41]
streamer	bakelite	2		0.4	[57]
streamer	bakelite	2		1.6	[37]
streamer	bakelite	2	3000	0.7	[36]
streamer	glass	2		0.4	[53]
streamer	bakelite	2		1.5	[43]
streamer	glass	2		0.45	[54]
streamer	bakelite	2		200 to 700	[55]
	bakelite + oil			1 to 13	

VIII. Ageing

Although there is already some satisfactory long-term operational experience in HEP experiments [43], where the irradiation dose is much larger than in cosmic ray physics, the difficulties encountered by the BABAR collaboration [44] will possibly motivate us in the near future to revise certain commonly accepted construction procedures.

IX. Time Resolution

A. Standard RPCs

A survey of recently published results concerning the time resolution of RPCs for MIPs as a function of the gap width are shown in Fig. 8.

Most standard 2-mm gap RPCs reach a resolution between 1 and 1.5 ns σ, independently of the operation mode. These results are normally taken using a simple leading-edge discrimination technique.

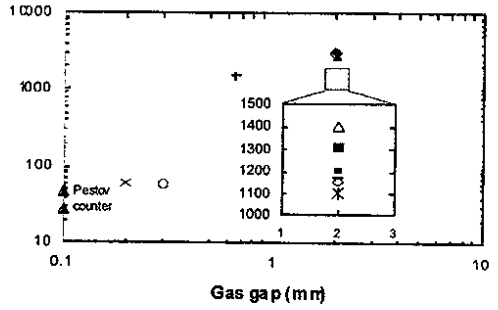

Fig. 8 Survey of recently published results concerning the time resolution of RPCs for MIPs as a function of the gap width. Most standard,2 mm gap,RPCs reach a resolution between 1 and 1.5 ns σ,independently of the operation mode. Thin gap timing RPCs reach a resolution of 50 ps σ. The time resolution of the Pestov counter is also shown for comparison [56]. (Legend: closed diamond [43], closed circle [53], closed triangle [56], large closed square[57], small closed square[67], + [39], x [46], open square [7], × [45], open triangle [65], [64], open diamond [63], *[62]; solid symbols -streamer mode, hollow symbols – avalanche mode).

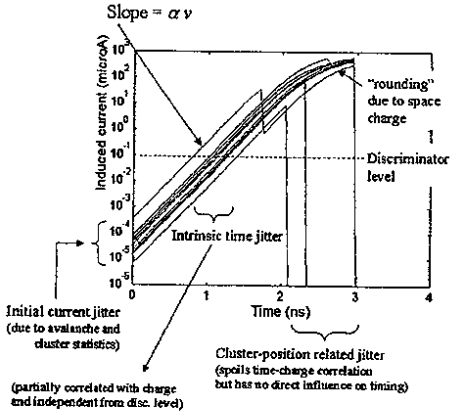

Fig. 9 Principle of operation of timing RPCs. The initial current grows exponentially in time until the discriminating level is reached. The time delay is independent from the position occupied by the initial charges, being the observed timing jitter dependent on the avalanche and cluster statistics and on the current growth rate αv

B. Timing RPCs

Timing RPCs have been recently developed [19] and reach currently a resolution of 50 to 60 ps σ for electrode areas ranging from 9 cm^2 ([7], [45]) to 1600 cm^2 [46].

An array of 32 counters with an area of 9 cm^2 each (of the type described in [7]) has been also successfully tested, showing in particular a very small amount of cross-talk ([47], [48]).

The possibility of simultaneous two-dimensional measurement of the avalanche position with millimetric accuracy and time measurement with a resolution of 50 ps σ has been recently demonstrated in single-gap counters ([49], [50]) aimed to be applied in relatively small and very accurate TOF systems.

The principle of operation of timing RPCs is illustrated in Fig. 9, based on the model described in [35]. The initial current grows exponentially in time until the discriminating level is reached. The time delay is independent from the position occupied by the initial charges in the gap, providing excellent timing. The observed timing jitter dependents on the variation of the initial current (avalanche and cluster statistics) and inversely on the current growth rateαv, where α is the First Townsend Coefficient and v is the electron drift velocity. It is also clear from the figure that in first approximation the timing accuracy should be independent of the discriminator level. Both this effect and the inverse dependence on αv have been experimentally confirmed.

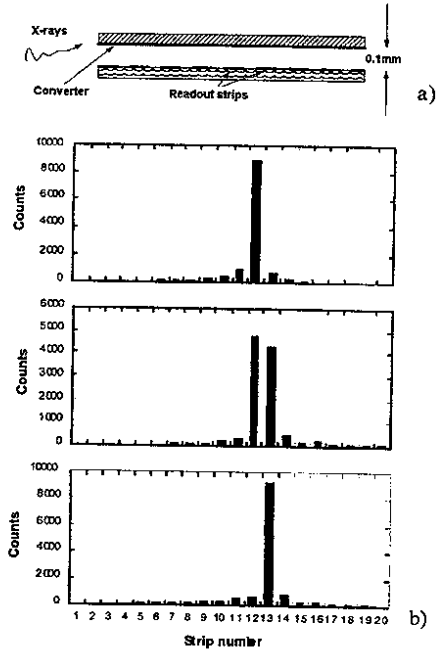

Fig. 10 a) Schematic drawing of a MicroRPC with a 100 μm gap, equipped with a solid X-ray converter and anodic strips placed at a pitch of 30 μm. b) results obtained under irradiation by a soft X-ray beam collimated by a 30 μm wide slit. Each histogram was obtained at successive slit positions offset by 15 μm in digital readout mode. The first and third histograms show that mostly a single strip was hit, yielding a resolution of at least 30 μm FWHM [9].

X. Position Resolution

A. Standard RPCs

The majority of RPC applications do not require the determination of the avalanche position with accuracy better than ~1 cm and therefore little effort has been made to optimize their position resolution.

However a small study has been done with soft X-rays in an 8 mm gap RPC equipped with 0.38 mm pitch strips below the anodic resistive plate, yielding the position of the induced charge profile centroid with a resolution of 115 μm FWHM [51].

B. MicroRPC

A 100 μm gap RPC equipped with a solid X-ray converter and anodic strips placed at a pitch of 30 μm has shown a position resolution of at least 30 μm FWHM in digital counting mode [9].

A schematic view of the device is shown in Fig. 10, along with the most important results. The events could be mostly concentrated in a single 30 μm wide strip.

The reasons for this result are the good localization of the primary charge given by the solid converter and the fact that most of the charge in the avalanche (due to its exponential growth in space) is developed very close to anode, yielding a very narrow induced charge profile.

XI. CONCLUSIONS AND OUTLOOK

Being robust (free of potentially damaging discharges) and affordable, standard RPCs enjoy today a wide acceptance in the HEP and Astroparticle community.

Two operation modes with similar efficiency and time resolution characteristics are available, with a tunable signal charge ranging from a few pC for the fast signal in avalanche mode to a range between 50 pC and a few nC in streamer mode.

The efficiency per gas gap for MIPs ranges from 45% for 0.1 mm gaps to 95% for the more common 2 mm gaps. Efficiencies above 99% are routinely reached by the use of 2 or more gaps sharing the same readout structure.

A good time resolution, from 1 to 2 ns σ, is also routinely achieved in either operation mode.

Present state-of-the-art counters reach counting rates up to a few kHz/cm^2 in avalanche mode and up to a few hundred Hz/cm^2 in streamer mode.

Recently some exciting developments have been made using special configurations.

Timing RPCs, made with glass electrodes that define several thin (0.2 to 0.3 mm) gas gaps, have reached a time resolution of 50 ps σ, opening perspectives for affordable high-granularity TOF counters. This performance is kept at least up to an electrode area of 800 cm^2 per readout channel and seems to be independent of the number of gas gaps (at least up to 5).

Very high rate operation (10 MHz/cm^2 at a gain of 5×10^4) was demonstrated for two different counter constructions, both featuring medium resistivity electrodes (10^4 to 10^7 Ω-cm).

An excellent position resolution of 30 μm FWHM for X-rays in digital readout mode was also recently reported.

These new developments may open new applications in medical imaging and reliable high-rate tracking of MIPs [41].

XII. ACKNOWLEDGEMENTS

Special acknowledgements are due to Vladimir Peskov and Archana Sharma for their encouragement and support.

XIII. REFERENCES

[1] R. Santonico and R. Cardarelli, "Development of Resistive Plate Counters", Nucl. Instr. Meth., vol. 187, pp. 377-380, 1981.

[2] V. V. Parkhomchuck, Yu. N. Pestov and N. V. Petrovykh, "A spark counter with large area", Nucl. Instr. Meth., vol. 93, pp. 269-276, 1971.

[3] Yu. N. Pestov, Proc 5th Int. Conf. on Instrumentation for Colliding Beam Physics, Novosibirsk, pp. 163-165, 1984.

[4] R. Cardarelli and R. Santonico, A. di Biagio and A. Lucci, "Progress in resistive plate counters", Nucl. Instr. Meth., vol. A263, pp. 20-25, 1988.

[5] R. Cardarelli, A. Di Ciaccio and R. Santonico, "Performance of a resistive plate chamber operating with pure CF3Br", Nucl. Instr. Meth., vol. A333, pp. 399-403, 1993.

[6] E. Cerron Zeballos, I. Crotty, D. Hatzifotiadou, J. Lamas-Valverde, S. Neupane, M. C. S. Williams, A. Zichichi, "A new type of resistive plate chamber: the multigap RPC", Nucl. Instr. Meth., vol. A374, pp. 132-135, 1996.

[7] P. Fonte, R. Ferreira-Marques, J. Pinhão, N. Carolino, A. Policarpo, "High-resolution RPCs for large TOF systems", Nucl. Instr. Meth., vol. A449, pp. 295, 2000.

[8] P. Fonte, N. Carolino, L. Costa, Rui Ferreira-Marques, S. Mendiratta, V. Peskov, A. Policarpo, " A spark-protected high-rate detector", Nucl. Instr. Meth., vol. A431, pp. 154-159, 1999.

[9] V. Peskov and P. Fonte, "Gain, Rate and Position Resolution Limits of Micropattern Gaseous Detectors", presented at the PSD99-5th International Conference on Position-Sensitive Detectors, London, England, 1999. Also preprint LIP/01-06 [Online]. Available: http://xxx. lanl. gov/abs/physics/0106017.

[10] M. Ambrosio, "Measurement of EAS thickness for individual events with RPCs in the GRES/COVER-PLASTEX experiment, Scientifica Acta, vol. 13, pp. 245-256, 1998.

[11] C. Aramo, "Arrival time measurement of muons in extensive air shower with bakelite RPC", Scientifica Acta, vol. 13, pp. 257-268, 1998.

[12] C. Bacci, K. Z. Bao, F. Barone, B. Bartoli, P. Bernardini, S. Bussino et al., "Results from the analysis of data collected with a 50 m RPC carpet at YangBaJing", Nucl. Instr. Meth., vol. A456, pp. 121-125, 2000.

[13] S. Dusini, D. Autiero, E. Borsato, R. Brugnera, L. Camilleri, F. Dal Corso et al., "Design and prototype tests of the RPC system for the OPERA spectrometers", presented at the "RPC2001 – 6th Workshop on Resistive Plate Chambers and Related Detectors", 26-27th November 2001, Coimbra, Portugal.

[14] G. Bencivenni , C. Gustavino, H. Menghetti, F. Murtas, L. Satta, N. Redaelli, G. Trinchero, "Performance of a test prototype for MONOLITH", Nucl. Instr. Meth., vol. A461, pp. 319-323, 2001.

[15] ALICE collaboration, "ALICE Muon Spectrometer technical design report", CERN, Geneva, report CERN/LHCC 99-22, 13 August 1999.

[16] ATLAS Muon collaboration, "ATLAS Muon Spectrometer Technical Design Report", CERN, Geneva, report CERN/LHCC 97-22, 5 June 1997.

[17] CMS Muon collaboration, "CMS muon technical design report", CERN, Geneva, report CERN/LHCC 97-32, 15 December 1997.

[18] LHCb Collaboration, CERN, Geneva, report "LHCb muon system technical design report", CERN-LHCC-2001-010, 28 May 2001.

[19] P. Fonte, A. Smirnitski and M. C. S. Williams, "A new high-resolution TOF technology", Nucl. Instr. Meth., vol. A443, pp. 201-204, 2000.

[20] M. Bogomilov, D. Dedovich, R. Dumps, F. Dydak, V. Gapienko, A. Semak et al., "The RPC time-of-flight system of the HARP experiment", presented at "RPC2001 – 6th Workshop on Resistive Plate Chambers and Related Detectors", 26-27th November 2001, Coimbra, Portugal.

[21] ALICE collaboration, "ALICE TOF technical design report", CERN/LHCC 2000-012, Geneva : CERN, 16 February 2000.

[22] G. Battistoni, P. Campana, V. Chiarella, U. Denni, E. Iarocci and G. Nicoletti, "Resistive cathode transparency", Nucl. Instr. Meth., vol. 202 pp. 459-464, 1982.

[23] H. Schöpf and B. Schnizer, "Theory describing cathode signals from charges moving in counters with a poorly conducting cathode", Nucl. Instr. Meth., vol. A323, pp. 338-344, 1992.

[24] M. Anelli, G. Bencivenni, G. Felici and L. Macro, "Glass electrode spark counters", Nucl. Instr. Meth., vol. A300, pp. 572-574, 1991.

[25] M. Yamaga, A. Abashian, K. Abe, K. Abe, P. K. Behera, S. Chidzik et al., "RPC systems for BELLE detector at KEKB", Nucl. Instr. Meth., vol. A456, pp. 109-112, 2000.

[26] G. Charpak and F. Sauli, "The multistep avalanche chamber: a new high-rate high-accuracy gaseous detector", Phys. Lett., vol. 78B, pp. 523-528, 1978.

[27] H. Raether, Electron Avalanches and Breakdown in Gases, London:Butterworths, 1964.

[28] S. C. Haydon, in Electrical Breakdown of Gases, ed. J. A. Rees, London: MacMillan, 1973, pp.146-172.

[29] I. Kitayama, H. Sakai, Y. Teramoto, S. Chinomi, Y. Inoue, E. Nakano, T. Takahashi, "Optical observation of discharge in resistive plate chamber", Nucl. Instr. Meth., vol. A424, pp. 474-478, 1999.

[30] A. Semak, V. Ammosov, V. Gapienko, A. Ivanilov, V. Koreshev, A. Kulemzin, Yu. Sviridov, V. Zaets, E. Gushin and S. Somov, "Properties of discharge in the narrow gap glass RPC", Nucl. Instr. Meth., vol. A456, pp. 50-54, 2000.

[31] P. Fonte, "A model of breakdown in parallel-plate detectors", IEEE Trans. Nucl. Sci., vol. 43, pp. 2135-2146, 1996.

[32] P. Camarri, R. Cardarelli, A. Di Ciaccio, R. Santonico, "Streamer suppression with SF 6 in RPCs operated in avalanche mode", Nucl. Instr. Meth., vol. A414, pp. 317-324, 1998.

[33] M. Abbrescia, A. Colaleo, G. Iaselli, F. Loddo, M. Maggi, B. Marangelli et al, "Progresses in the simulation of Resistive Plate Chambers in avalanche mode", Nucl. Phys. B, vol. 78, pp. 459-465, 1999.

[34] P. Fonte and V. Peskov, "High-Resolution TOF with RPCs", Nucl. Instr. Meth., vol. A477, pp.17-22, 2002.

[35] P. Fonte, "High-Resolution Timing of MIPs with RPCs – a Model", Nucl. Instr. Meth., vol. A456, pp. 6-11, 2000.

[36] R. Arnaldi, A. Baldit, V. Barret, N. Bastid, G. Blanchard, E. Chiavassa, et al., "Study of the resistive plate chambers for the ALICE Dimuon Arm", Nucl. Instr. Meth., vol. A 456, pp. 73-76, 2000.

[37] C. Bacci, K. Z. Bao, F. Barone, B. Bartoli, P. Bernardini, R. Buonomo and the ARGO-YBJ Collaboration, "High altitude test of RPCs for the Argo YBJ experiment", Nucl. Instr. Meth., vol. A443, pp. 342-345, 2000.

[38] V. Koreshev, V. Ammosov, A. Ivanilov, Yu. Sviridov, V. Zaets and A. Semak, "Operation of narrow gap RPC with tetrafluoroethane based mixtures", Nucl. Instr. Meth., vol. A456, pp. 46-49, 2000.

[39] P. Colrain, G. Corti, L. de Paula, M. Gandelman, J. Lamas-Valverde, B. Marechal, D. Moraes, E. Polycarpo, B. Schmidt, T. Schneider and A. Wright, "Performance of a Multigap RPC prototype for the LHCb Muon system", Nucl. Instr. Meth., vol. A456, pp. 62-66, 2000.

[40] C. Iacobaeus, M. Danielsson, P. Fonte, T. Francke, J. Ostling, V. Peskov, "Sporadic Electron Jets from Cathodes – The Main Breakdown-Triggering Mechanism in Gaseous Detectors", presented at the 2001 IEEE Nuclear Science Symposium, 4-10 November, San Diego, California, USA, 2001.

[41] T. Francke, P. Fonte, V. Peskov and J. Rantanen, "Potential of RPCs for tracking", presented at the RPC2001–6th Workshop on Resistive Plate Chambers and Related Detectors, 26-27th November 2001, Coimbra, Portugal.

[42] Y. Ivaniouchenkov, P. Fonte, V. Peskov, B. D. Ramsey, "Breakdown limit studies in high-rate gaseous detectors", Nucl. Instr. Meth., vol. A422, pp. 300-304, 1999.
[43] A. Aloisio, M. G. Alviggi, S. Patricelli, C. Sciacca, G. Carlino, N. Cavallo, et al., "Long-term performance of the L3 RPC system", Nucl. Instr. Meth., vol. A456, pp. 113-116, 2000.
[44] D. Strom, "Resistive Plate Chamber Performance in the Babar IFR System", presented at the 2001 IEEE Nuclear Science Symposium, 4-10 November, San Diego, California, USA, 2001.
[45] A. Akindinov, F. Anselmo, M. Basile, E. Cerron Zeballos, L. Cifarelli et al., "The multigap resistive plate chamber as a time-of-flight detector", Nucl. Instr. Meth., vol. A456, pp. 16-22, 2000.
[46] A. Blanco, R. Ferreira-Marques, C. Finck, P. Fonte, A. Gobbi, A. Policarpo and M. Rozas, "A Large Area Timing RPC", Nucl. Instr. Meth. A, accepted for publication. Also preprint LIP/01-04 [Online]. Available: http://xxx. lanl. gov/abs/physics/0103086.
[47] A. Akindinov, P. Fonte, F. Formenti, V. Golovin, W. Klempt, A. Kluge et al., "A four-gap glass-RPC time of flight array with 90 ps time resolution", IEEE Trans. Nucl. Sci., vol. 48, n°.5, pp.1658-1663, 2001.
[48] M. Spegel and the ALICE Collaboration, "Recent progress on RPCs for the ALICE TOF system", Nucl. Instr. Meth., vol. A453, pp. 308, 2000.
[49] A. Blanco, R. Ferreira Marques, Ch. Finck, P. Fonte, A. Gobbi, S. K. Mendiratta, J. Monteiro, A. Policarpo and M. Rozas, "Development of large area and of position sensitive timing RPCs", Nucl. Instr. Meth., vol. A478, pp.170-175, 2002.
[50] A. Blanco, R. Ferreira Marques, Ch. Finck, P. Fonte, A. Gobbi, A. Policarpo, "Single-Gap Timing RPCs with Bidimensional Position Sensitive Readout for Very Accurate TOF systems", presented at the the RPC2001 – 6th Workshop on Resistive Plate Chambers and Related Detectors, 26-27th November 2001, Coimbra, Portugal.
[51] E. Ceron Zeballos, I. Crotty, D. Hatzifotiadou, J. Lamas Valverde, M. C. S. Williams, A. Zichichi, P. Fonte and V. Peskov, Nucl. Instr. Meth. A392, pp. 150-154, 1997.
[52] A. Zallo, "The BABAR RPC system", Nucl. Instr. Meth., vol. A456, pp. 117-121, 2000.
[53] K. Abe, K. Abe, H. Hanada, H. Haitani, Y. Hoshi, Y. Inoue, "Glass RPC module for the BELLE Endcap K_L/μ Detector", Scientifica Acta, vol. 13, pp. 281-293, 1998.
[54] K. Abe, F. Handa, I. Higuchi, Y. Hoshi, N. Kawamura, Y. Mikami, et al., "Performance of glass RPC operated in streamer mode with SF_6 gas mixture", Nucl. Instr. Meth., vol. A455, pp. 397-404, 2000.
[55] M. Abbrescia, A. Colaleo, G. Iaselli, M. Maggi, B. Marangelli, S. Natali et al., Effect of the linseed oil surface treatment on the performance of resistive plate chambers", Nucl. Instr. Meth., vol. A394, pp. 13-15, 1997.
[56] Yu. N. Pestov, H. R. Schmidt and B. Schreiber, "Timing performance of spark counters and photon feedback", Nucl. Instr. Meth., vol. A456, pp. 11-15, 2000.
[57] B. Bartoli, R. Buonomo, E. Calloni, S. Catalanotti, B. D'Ettore Piazzoli, G. Di Sciascio and M. Iacovacci, "Study of RPC gas mixtures for the ARGO-YBJ experiment", Nucl. Instr. Meth., vol. A456, pp. 35-39, 2000.
[58] V.V.Ammosov, V.A.Gapienko, V.F.Konstantinov, Yu.M.Sviridov and V.G.Zaets, "Study of avalanche mode operation of resistive plate chambers with different gas gap structures", Nucl. Instr. Meth., vol. A441, pp. 348-358, 2000.
[59] M.Adinolfi, G.Carboni, R.Messi, L.Pacciani, L.Paoluzi and E.Santovetti "Performance of low-resistivity single and dual-gap RPCs for LHCb", Nucl. Instr. Meth., vol. A456, pp.95-99, 2000.
[60] M.Cwiok, W. Dominik, M.Górski and J.Krolikov, "The performance of RPCs with bakelite electrodes of various resistivity under high radiation fluxes", Nucl. Instr. Meth., vol. A456, pp.87-90, 2000.
[61] G.Aielli, P.Camarri, R.Cardarelli, A.Di Ciaccio, L.Di Stante, B.Liberti, A.Paoloni and R.Santonico, "Response uniformity of a large size RPC", Nucl. Instr. Meth., vol. A456, pp.40-45, 2000.
[62] G.Aielli, P.Camarri, R.Cardarelli, V.Chiostri, R.De Asmundis, A.Di Ciaccio et al., "Performance of a large-size RPC equipped with the ATLAS front-end electronics at X5-GIF irradiation facility", Nucl. Instr. Meth., vol. A456, pp.77-81, 2000.
[63] M.Abbrescia, S.Altieri, G.Belli, G.Bruno, A.Colaleo, I.Crotty et al., "Performance of the RPC station prototype for the CMS barrel detector", Nucl. Instr. Meth., vol. A456, pp.103-108, 2000.
[64] S.H. Ahn et al., "Performance of a large forward resistive plate chamber for the CMS/LHC under high radiation environment ", Nucl. Instr. Meth., vol. A 469, pp.323-330, 2001.
[65] J.Ying, Y.L.Ye, Y.Ban, H.T.Liu, Z.M. Zhu, Z.Y.Zhu, T.Chen, J.G.Ma and S.J.Qian, "Beam test results of a resistive plate chamber made of Chinese bakelites", Nucl. Instr. Meth., vol. A459, pp.513-522, 2001.
[66] Y.H.Chang, D.Chen, E.S. Hafen, P.Haridas, I.A.Pless, J.Tomasi et al., "A study of meter size RPCs for large area detectors", Nucl. Instr. Meth., vol. A 349, pp.47-55, 1994.
[67] Gustavino, M.D'Incecco, E. Tatananni , G.C. Trinchero, "A glass resistive plate chamber for large experiments", Nucl. Instr. Meth., vol. A457, pp. 558-563, 2001.
[68] E. Cerron Zeballos, D. Hatzifotiadou, J. Lamas Valverde, E. Platner, J. Roberts, M.C.S. Williams, A. Zichichi, "Micro-streamers and the micro-gap Resistive Plate Chamber", Nucl. Instr. Meth., vol. A411, pp.51-62, 1998.
[69] G. Carlino, "The RPC trigger system of L3: history and current status", Scientifica Acta, vol. 13, pp. 269-280, 1998.

AN ADVANCED STUDY OF SILICON PHOTOMULTIPLIER

P. Buzhan, B. Dolgoshein*, A. Ilyin, V. Kantserov, V. Kaplin, A. Karakash, A. Pleshko, E. Popova, S. Smirnov, Yu. Volkov

Moscow Engineering and Physics Institute, Moscow, Russia

L. Filatov and S. Klemin

""Pulsar" Enterprise, Moscow, Russia

F. Kayumov

Lebedev Physical Institute, Moscow, Russia

ABSTRACT

An advanced study of new photo detector - Silicon Photomultiplier (SiPM) is presented. SiPM consists of many ($\sim 10^3$ mm^{-2}) silicon micro pixels, which are independent photon micro-counters working in limited Geiger mode with a gain of 10^6. The SiPM output signal is a sum of the signals from a number of pixels fired by photons. The main features of SiPM are: low excess noise factor, the photon detection efficiency at the level of vacuum PMT, low bias voltage ($\sim$24V). The timing of the SiPM is about 30 ps for 10 photoelectrons. The possibilities of SiPM applications based on experimental tests are demonstrated: sci fiber readout, scintillator-shifter system readout, and possible application for hadron calorimeters.

*Corresponding author. E-mail address: boris@mail.cern.ch

1 Introduction

The Silicon Photomultiplier (SiPM) is a multipixel semiconductor photodiode, where the pixels are joint together on common silicon substrate[1]. Each SiPM pixel operates in limited Geiger mode, under bias voltage of 10-20% more than breakdown voltage, so each carrier generated by photons or thermally gives rise to a Geiger-type discharge. This Geiger discharge is stopped when the voltage goes down below breakdown value due to external resistor R on each pixel (typical R value is about 100-200 kΩ). This resistor also serves as a decoupling element between the individual pixels because $C_{pixel} \cdot R_{pixel} \sim 10^{-8} s \gg t_{discharge}$, where discharge time $t_{discharge} < 1$ ns.

Actually, each SiPM pixel operates as an independent photon Geiger micro-counter (like a single pixel device - single photon avalanche diode SPAD[2]), and the pixel Geiger signal does not depend on a triggered carrier number, which fires the pixel ("Geiger mode"). Single pixel gain is determined by the charge accumulated in pixel capacity C_{pixel}: $Q_{pixel} = C_{pixel} \cdot (V_{bias} - V_{breakdown})$. Typically, $C_{pixel} \simeq$100 fF, and V_{bias}-$V_{breakdown} \simeq$ a few volts, so $Q_{pixel} \simeq$ few times 100 pC and the single pixel "gain" is about 10^6, i.e., the same order as vacuum PMT gain. The pixel size is of 15 to 70 μm, and the total number of SiPM pixels is 100-4000 mm^{-2}. Because all SiPM pixels work together on common load, the output signal is a sum of the signals from all pixels fired. So such a number of pixels, where each element operates digitally as a binary device, works as an analogue detector, which can measure light intensity.

2 SiPM Description and Performance

2.1 SiPM topology

Figure 1a shows, as an example, the microphotograph of SiPM with pixel size 42x42 μm^2, and a total pixel number m=576 on the area of 1 mm^2. The SiPM topology is shown in Fig. 1b. A few micron epitaxy layer on low resistive p substrate forms the drift region with low built-in electric field (see Fig. 1c). The thin depletion region (0.7-0.8 μm) between the p$^+$ and n$^+$ layers with very high electric field (3 - 5)·10^5 V/cm is created, where the conditions for Geiger mode discharge take place ($V_{bias} > V_{breakdown}$). The electrical decoupling between the adjacent pixels is provided by polysilicon resistive strips and uniformity of the electric field within a pixel by the n$^-$ guard rings around each pixel (Fig. 1a,b). All 576 pixels are connected by common Al strips, in order to readout the SiPM signal.

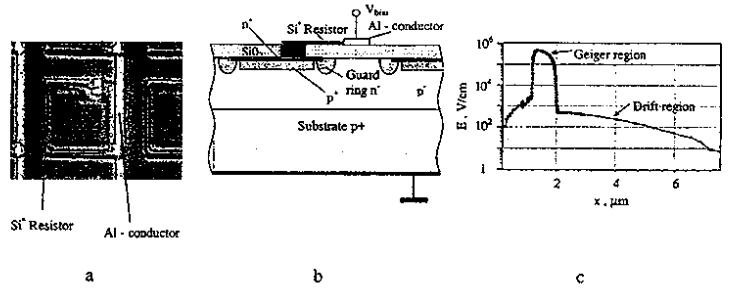

Figure 1: (a) Silicon photomultiplier microphotograph, (b) topology and (c) electric field distribution in epitaxy layer.

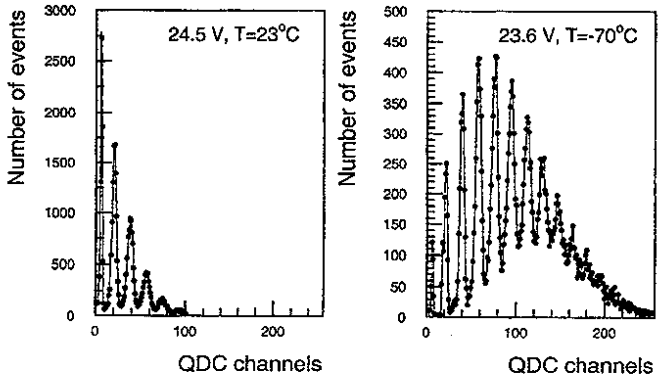

Figure 2: SiPM pulse height spectra.

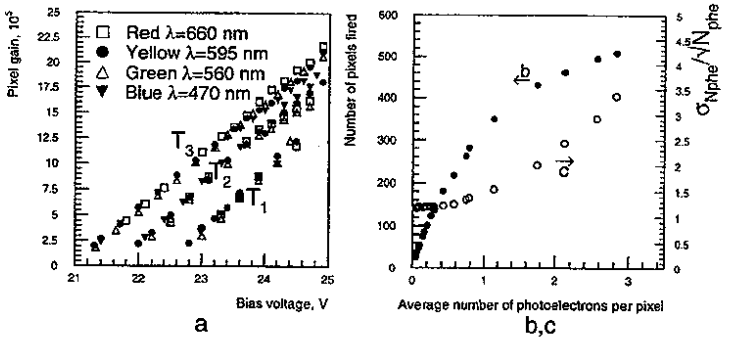

Figure 3: SiPM single pixel gain (a) for different temperatures: T_1=+22°C, T_2=-22°C, T_3=-61°C; (b) SiPM signal saturation for m=576, and (c) signal dispersion.

2.2 SiPM Pulse Height Spectrum

The SiPM pulse height spectra from a low-intensity light emission diode (LED) source are shown in Fig. 2, for two temperatures 23°C and -70°C. We can conclude from Fig. 2:

- single (double, triple, etc.) photoelectron(s) peak(s) is(are) clearly visible;
- one very easily can estimate the SiPM gain, using single photoelectron peak, which obviously corresponds to the single pixel fired: $Gain = Q_{one\ pixel}/e$, where e is the electron charge;
- pixel-to-pixel gain variation is rather small, i.e., the pixel capacitance is quite uniform: $\sigma_1/S_1 \simeq$ 10%, where S_1 and σ_1, are single pixel signal and its dispersion, respectively;
- SiPM excess noise factor (ENF), responsible for pixel-to-pixel gain variation $ENF = 1+\sigma_1^2/S_1^2$ is very small;
- the contribution of electronics noise (pedestal width) is also very small;
- SiPM gain and photon detection efficiency (compare Figs. 2a and b) are overvoltage $\Delta V = V_{bias} - V_{breakdown}$ and temperature dependent.

2.3 Sensitivity of the SiPM Gain

Figure 3a shows the SiPM gain vs V_{bias} dependence for different temperatures and light wavelengths. The experimental points in Fig. 3a have been obtained by measuring the single photoelectron peak positions (see Fig. 2). The voltage and temperature sensitivity of the SiPM gain can be obtained from Fig. 3a data and is rather weak compared, for instance, to standard avalanche photodiodes (APD). Indeed, we obtain the following dependencies at V_{bias}=24.5V (gain $\simeq 1.5{\cdot}10^6$):

- Gain variation vs overvoltage $dG/G \simeq 7 \cdot dV_{bias}/V_{bias}$, which gives $dG/G \simeq$3% for dV_{bias}=0.1 V;
- Gain variation vs temperature $dG/G \simeq 1.3 \cdot dT/T(°K)$, which gives dG/G=0.5% for dT=1° and T=-20°C.

Such a voltage and temperature variations of the SiPM gain have to be compared with the same values for avalanche photodiodes[3]: $dG/G = 75 \cdot dV/V_{bias}$ and $dG/G = 17 \cdot dT/T$ for an APD gain of 100.

The low voltage and temperature sensitivity of SiPM gain is an important practical advantage compared to the APD.

2.4 SiPM Dynamic Range

The SiPM dynamic range is limited due to the finite total pixel number m at $N_{ph} \cdot \varepsilon/m < 1$, where N_{ph} is the number of photons, and ε - the photon detection efficiency. This means that the average number of photoelectrons per one pixel should be small enough. The finite pixel number m results in the saturation of the SiPM signal with increased light intensity (or the average number of photoelectron per each pixel) (see Fig. 3b). The signal dispersion, in terms of the number of photoelectrons, can be calculated using this curve. Figure 3c shows the deviation of the signal dispersion from Poissonian value $\sigma = \sqrt{N_{phe}} = \sqrt{N_{ph} \cdot \varepsilon}$, as a function of light intensity. As can be seen from Fig. 3c the value of σ is quite close to Poissonian for $N_{phe}/m \leq 0.6$, and dramatically increases for large N_{phe}/m values due to saturation of the SiPM signal.

In conclusion, the SiPM dynamic range is determined by deterioration of the signal dispersion at $N_{phe} \geq 0.6{\cdot}m$. The increase of total pixel number m seems technologically possible up to ~4000 mm^{-2}; therefore, the SiPM dynamic range of up to $2.5{\cdot}10^3$ phe/mm^2 is feasible.

2.5 SiPM Photon Detection Efficiency

The SiPM photon detection efficiency is $\varepsilon = QE \cdot \varepsilon_G \cdot A_{pixels}/A_{total}$, where QE is the quantum efficiency (typically 0.5-0.8, wavelength dependent), A_{pixels}/A_{total} is the so-called geometrical efficiency that is a fraction of total the SiPM area, occupied by active pixel area A_{pixel} and ε_G is probability

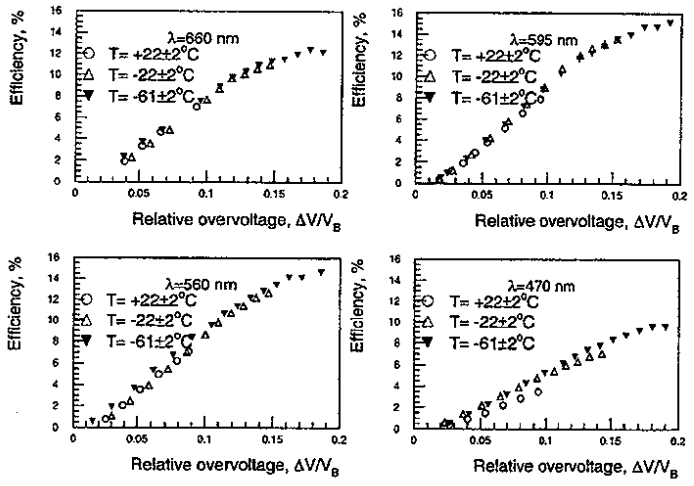

Figure 4: SiPM photon detection efficiency for different temperatures and light wavelengths.

for a carrier created in active pixel area to initiate a Geiger-mode discharge. The photon detection efficiency has been measured using a different wave-length light emission diodes and the calibrated PMT and is shown in Fig. 4 as function of relative overvoltage $OV = (V_{bias} - V_{breakdown})/V_{breakdown}$. One can see, that efficiency for the visible light is comparable to standard vacuum PMT with bial-cali photocathode for green and blue light and even better in yellow-red region. The SiPM photon detection efficiency achieved is significantly higher compared to our previous paper[1]. The SiPM performance is limited for $OV > 1.15$ - 1.20 due to the increase of dark noise rate.

2.6 SiPM Noise

The electronics noise ib SiPMs is negligibly small because of very high gain ($\sim 10^6$), in contrast to standard avalanche photodiodes, where the gain is typically 100-200. Actually, the level of electronics noise is less than 0.1 electrons (see Fig. 2, pedestal width).

The main source of noise limiting the SiPM performance is dark noise rate, which originates from the carriers created thermally in sensitive volume and also due to the effects of high electric fields[4]. The SiPM dark rate decreases with temperature from a few MHz/mm^2 (room temperature) to ~1kHz/mm^2 (at 100°K).

Such a dark noise rate limits SiPM performance at temperatures above 0°C, especially for large sensitive area (~1 cm^2), and needs to be reduced by improving pixel production technology. However, SiPM's dark noise rate limits SiPM performance only in detection of very small light intensities (one or a few photoelectrons), and it does not affect in the case of larger light signals.

2.7 Timing by SiPM

The development of the Geiger-type discharge, for a very small width of depletion region, is very fast (a few hundred picoseconds). The typical rise time observed is ~1 ns, the decay time is determined by the time constant $C_{pixel} \cdot R_{pixel}$=30 ns, thus, the recovery time of a single SiPM pixel is <100 ns and a much smaller recovery time for the whole SiPM is expected.

Timing with SiPMs has been studied using a very fast red-laser diode (λ=670 nm, light signal width of 40 ps). Figure 5a shows the time resolution (r.m.s.) as a function of the number of pixels fired for photons absorbed in the Geiger region. One observes very good timing resolution, which follows the Poissonian law $1/\sqrt{N_{pixels\ fired}}$. Figure 5b shows a shift of the time distributions for a displacement in space of the laser source. There is a clear separation between the peaks for the displacement of 30 mm with an r.m.s. value of about 7.5 mm.

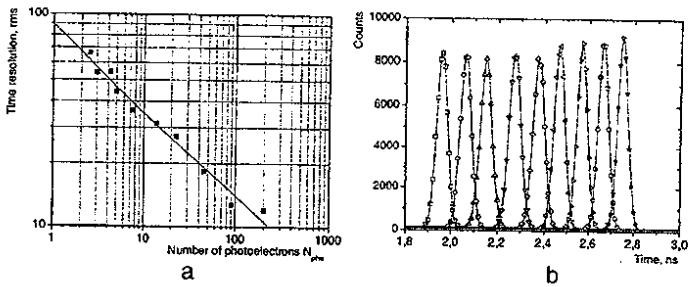

Figure 5: (a) SiPM time resolution and (b) time spectra for different positions of the light source shifted by 30 mm.

3 Experimental Tests for Possible SiPM Applications

3.1 Scintillation Fiber Detector: SiPM vs APD Comparison

The relativistic particle detection by scintillation fiber has been studied using an Sr^{90} β-source and multicladding Kuraray scintillation fiber SCSF-3HF (1500)M with a core diameter of 0.94 mm, an emission peak of 530 nm, a decay time of 7 ns, and 1/e length of >4.5 m.

The results of the measurements are shown in Fig. 6, together with the results obtained with the the APD on a similar measurement, (a gain of 100-500, and a quantum efficiency QE of 70%)[5]. The SiPM has a much lower photon detection efficiency (15%); however due to: 1) practical absence of electronics noise and 2) a lower ENF factor, the SiPM performs approximately as good as the APD (in terms of signal/noise ratio).

3.2 Plastic Scintillator + Wavelength Shifter (WLS) Readout: SiPM vs APD Comparison

The plastic scintillator with a wavelength shifter (WLS) readout has become a more and more popular device, because of the need to readout a very large number of scintillators (e.g., preshower[6] or tile calorimeters[7]). In addition, due to the small space available and the need to perform in a high magnetic field, the usage of PMT readout is difficult. Therefore, the Si-based photodetectors (like the APD) look more promising.

We have carried out test measurements with a plastic scintillator and a WLS readout* using

*We used the scintillation counter and WLS fiber readout produced by V.Semenov (IHEP).

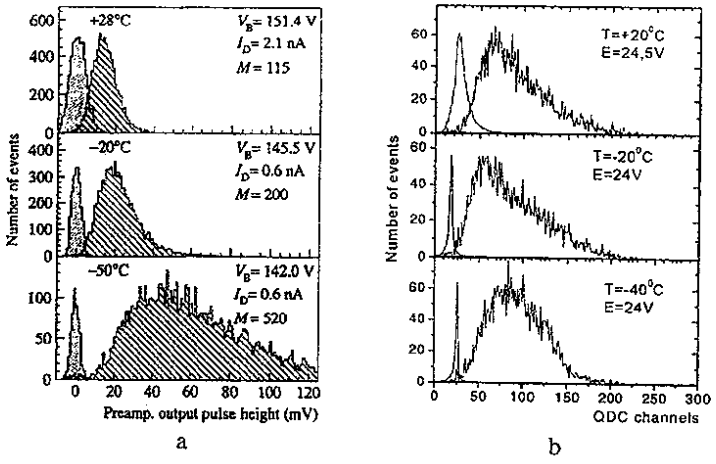

Figure 6: Comparison of (a) APD and (b) SiPM spectra from relativistic particles detected by scintillation fiber.

SiPM. Figure 7 shows the test results for a plastic scintillator, 14x14 cm^2 and 4 mm thickness, for minimum ionizing particles (cosmic muons and electrons from an Sr^{90} source). For optical readout, we used fiber with 1 mm diameter and WLS (λ=494 nm), and a length of 1.5 m. The loop of the WLS fiber was embedded in a plastic body, with one end of the fiber covered by an aluminized mirror in order to increase the light collection, the other one was connected to the SiPM. The results for the SiPM readout are compared in Fig.7 with similar APD results[6], where scintillation light detection was used. We can see that despite the lower SiPM photon detection efficiency, the MIP detection looks favorably to the SiPM (again, due to a much lower electronics noise and ENF value).

3.3 TESLA Hadron Tile Calorimeter Readout Using SiPMs

We have studied the possibility of a tile scintillator and a WLS fiber readout with an Si photomultiplier, for example, for the Tesla Hadron Tile Calorimeter experiment[8].

The calorimeter has a tower-like scintillator tile structure; each tower consists of scintillator cells with a minimum three scintillator tiles in one cell (front side), and a maximum of 7 scintillator tiles in one cell (back side). Each 5-mm thick tile scintillator is readout by a WLS fiber with 1 mm

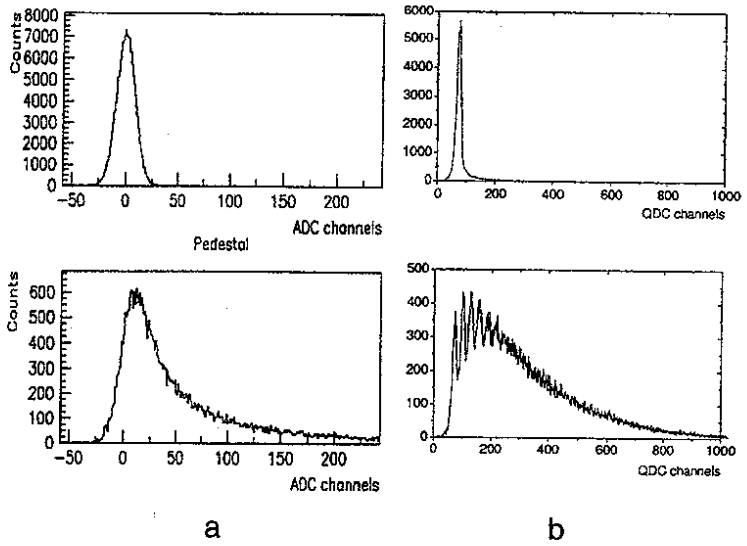

Figure 7: Comparison of APD (a) and SiPM (b) spectra from relativistic particles detected by plastic scintillator + WLS.

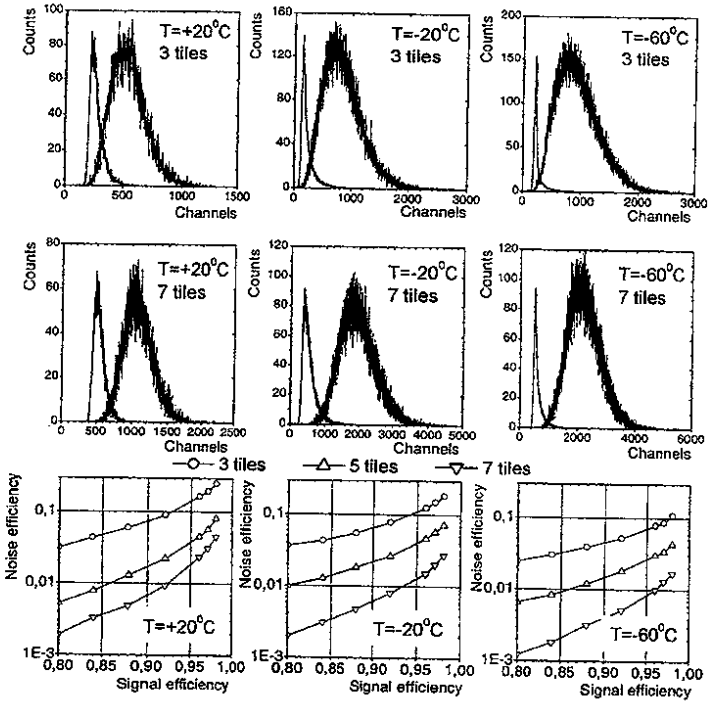

Figure 8: SiPM performance for TESLA HCAL (see text).

in diameter.

The TESLA hadron calorimeter required a dynamic range of photodetectors as determined by[8]:

- minimal signal: MIP (muons, used for calibration purposes), expected number of scintillator photons: n_{min}=60/3tiles=20photons/mm^2 of SiPM;
- maximal signal: high-energy jet, the expected number of photons is n_{max}=3.6·10^4/7tiles $\simeq$ 5·10^3 photons/mm^2 of SiPM.

To decrease the impact of the SiPM signal saturation (see Fig.3b) and meet the $n_{max} \cdot \varepsilon/m < 0.6$ requirement, we need to have the number of SiPM pixels per 1mm^2 $m \geq 5 \cdot 10^3 \cdot 0.15/0.6 \simeq 1200$ for photon detection efficiency of ε_{ph}=0.15. The SiPM is undergoing modifications to increase the number of pixels to 2500 mm^{-2} at "Pulsar" enterprise (Moscow). In order to demonstrate the feasibility of TESLA hadron calorimeter calibration by an MIP, we used the experimental data for one tile and superimposed 3, 5, or 7 tiles together. The results of such a superposition, which simulates the calorimeter cells response with 3 and 7 tiles, are shown in Fig.8. We can see a good MIP signal/noise ratios (shown in bottom half of Fig.8) which looks promising for utilization within the cell structure of the calorimeter.

4 Conclusions

In conclusion a comparison in Table 1 shows the SiPM characteristics and performance of typical present photodetectors, such as vacuum phototubes (PMT), Si avalanche photodiodes (APD), and hybrid photodetectors (HPD).

As can be seen, Si Photomultiplier appears to be good candidate to complement a wide range of photodetectors.

Acknowledgments

The authors would like to thank Prof. R.Klanner for his close attention and invaluable support during the SiPM research and development work.

This work was supported by the International Science and Technology Center, grant ISTC 1275-99.

Table 1:

	PMT	APD	HPD	SiPM
Photon detection efficiency:				
blue	20%	50%	20%	12%
green - yellow	a few %	60-70%	a few %	15%
red	<1%	80%	<1%	15%
Gain	10^6-10^7	100-200	10^3	10^6
High voltage	1-2 kV	100-500 V	20 kV	25 V
Operation in the magnetic field	problematic	OK	OK	OK
Threshold sensitivity S/N$\gg$1	1 ph.e.	~10 ph.e.	1 ph.e.	1 ph.e.
Timing /10 ph.e.	~100 ps	a few ns	~100 ps	30 ps
Dynamic range	~10^6	large	large	~10^3/mm^2
Complexity	high (vacuum, HV)	medium (low noise electronics)	very high (hybrid technology, very HV)	relatively low

References

[1] G. Bondarenko et al, NIM A242(2000)187 and references therein.

[2] F. Zappa et al, Opt. Eng. 35(4) (1996)938,
S. Cowa et al, J. Appl. Phys. 35(1996)1956 and references therein.

[3] A. Karar et al., NIM A428(1999)413.

[4] G. Vincent et al, J. Appl. Phys. 50(1979)5984.

[5] T. Okusawa et al., NIM A459(2001)441.

[6] C. Cheshkov et al., NIM A440(2000)38.

[7] HCAL Technical Design Report, CERN/LHCC 97-31, CMS TDR2, 1997.

[8] Tesla Technical Design Report, v.3,4, DESY 2001-011, March 2001.